

Thermoelectric Precession in Turbulent Magnetoconvection

Yufan Xu^{1,†}, Susanne Horn^{1,2} and Jonathan M. Aurnou¹

¹Department of Earth, Planetary, and Space Sciences, University of California, Los Angeles, CA 90095, USA

²Centre for Fluid and Complex Systems, Coventry University, CV1 2NL, Coventry, UK

(Received xx; revised xx; accepted xx)

We present laboratory measurements of the interaction between thermoelectric currents and turbulent magnetoconvection. In a cylindrical volume of liquid gallium heated from below and cooled from above and subject to a vertical magnetic field, it is found that the large scale circulation (LSC) can undergo a slow axial precession. Our experiments demonstrate that this LSC precession occurs only when electrically conducting boundary conditions are employed, and that the precession direction reverses when the axial magnetic field direction is flipped. A thermoelectric magnetoconvection (TEMC) model is developed that successfully predicts the zeroth-order magnetoprecession dynamics. Our TEMC magnetoprecession model hinges on thermoelectric current loops at the top and bottom boundaries, which create Lorentz forces that generate horizontal torques on the overturning large-scale circulatory flow. The thermoelectric torques in our model act to drive a precessional motion of the LSC. This model yields precession frequency predictions that are in good agreement with the experimental observations. We postulate that thermoelectric effects in convective flows, long argued to be relevant in liquid metal heat transfer and mixing processes, may also have applications in planetary interior magnetohydrodynamics.

Key words:

1. Introduction

The classical set-up for magnetoconvection (MC) is that of Rayleigh-Bénard convection (RBC) in an electrically-conductive fluid layer occurring in the presence of an externally imposed magnetic field (e.g., Chandrasekhar 1961; Nakagawa 1955). The electrically conducting fluid layer is heated from below and cooled from above, typically with the assumption that the top and bottom horizontal boundaries are isothermal and electrically insulating. The imposed magnetic field is usually vertically- (e.g., Cioni *et al.* 2000; Aurnou & Olson 2001; Zürner *et al.* 2020) or horizontally-oriented (Tasaka *et al.* 2016; Vogt *et al.* 2018*b*). MC is employed as an idealized model for many physical systems (e.g., Weiss & Proctor 2014). In geophysics, MC is considered an essential sub-system of the thermocompositionally driven turbulent convection that generates the magnetic fields in molten metal planetary cores (e.g., Jones 2011; Roberts & King 2013; Aurnou & King 2017; Moffatt & Dormy 2019). In astrophysics, MC is associated with the sunspot umbra structure, where the strong magnetic field suppresses the

† Email address for correspondence: yufanxu@g.ucla.edu

thermal convection in the outer layer of the Sun and other stars (e.g., Proctor & Weiss 1982; Schüssler & Vögler 2006; Rempel *et al.* 2009). MC is also related to the X-ray flaring activities on magnetars with extremely large magnetic flux densities estimated from 10^9 to 10^{11} T (Castro-Tirado *et al.* 2008). Furthermore, MC has an essential role in numerous industrial and engineering applications such as crystal growth (e.g., Moreau 1999; Rudolph 2008), design of liquid-metal-cooled blankets for nuclear fusion reactors (e.g., Barleon *et al.* 1991; Abdou *et al.* 2001; Salavy *et al.* 2007) as well as induction heating, casting (e.g., Taberlet & Fautrelle 1985; Davidson 1999), and liquid metal batteries (Kelley & Weier 2018; Cheng *et al.* 2021).

In sharp contrast to the ideal theoretical MC system, liquid metals employed in many laboratory and industrial MC systems have different thermoelectric properties from the boundary materials. This is also the case in natural systems where the properties significantly differ across a material interface, such as at the Earth’s core-mantle boundary (e.g., Lay *et al.* 1998; Mao *et al.* 2017; Mound *et al.* 2019). When an interfacial temperature gradient is present, thermoelectric currents are generated that can form current loops across the interface (e.g., Shercliff 1979; Jaworski *et al.* 2010). When in the presence of magnetic fields that are not parallel to the currents, Lorentz forces arise that can stir the liquid metal (Jaworski *et al.* 2010). Such phenomena can be explained by the thermoelectric magnetohydrodynamics (TE-MHD) theory first developed by Shercliff (1979), which focussed on forced heat transfer in nuclear fusion blankets. Although other applications of TE-MHD exist in solidification processes and crystal growth (e.g., Boettinger *et al.* 2000; Kao *et al.* 2009), we are unaware of any previous applications of TE-MHD where the boundary thermal gradients are set by the convection itself (cf. Zhang *et al.* 2009), as occurs in the experiments presented here.

Our laboratory experiment focuses on the canonical configuration of turbulent MC in a cylindrical volume of liquid gallium in the presence of vertical magnetic fields and with different electrical boundary conditions. Three behavioral regimes are identified primarily using sidewall temperature measurements: i) a turbulent large-scale circulation ‘jump rope vortex (JRV)’ regime in the weak magnetic field regime (Vogt *et al.* 2018a); ii) a magnetoprecessional (MP) regime in which the large-scale circulation (LSC) precesses around its vertical axis is found for moderate magnetic field strengths and electrically conducting boundary conditions; iii) a multi-cellular magnetoconvection (MCMC) regime is found in the highest magnetic field strength cases. Although this is the first systematic study of the magnetoprecessional mode, this is not the first time that it has been experimentally observed. This behavior was first observed in our laboratory in the thesis experiments of Grannan *et al.* (2017). In addition, what appears to be a similar precession was reported in the MC experiments of Zürner *et al.* (2020).

The rest of the paper is organized as follows. Section 2.1 introduces the fundamentals of thermoelectric effects. Section 2.2 presents the governing equations and non-dimensional parameters that control the TEMC system. Section 2.3 reviews the established stability analysis and previous research related to the MC system. Section 3 addresses the experimental setup, the diagnostics used, and the physical properties of our working fluid, liquid gallium. Section 4 shows the experimental results with electrically-insulating boundary conditions. Section 5 presents the results of experiments made with electrically-conducting boundary conditions and the appearance of the magnetoprecessional mode. Following these laboratory results, in section 6, we develop an analytical model of the magnetoprecessional mode driven by thermoelectric currents generated by horizontal temperature gradients that exist along the top and bottom electrically-conducting boundaries. Finally, Section 7 contains a discussion of our findings and potential future applications.

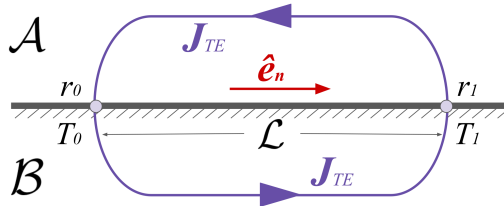


FIGURE 1. A thermoelectric current loop, \mathbf{J}_{TE} , forms across two different conducting materials \mathcal{A} and \mathcal{B} with a horizontal temperature gradient in the $\hat{\mathbf{e}}_n$ -direction. The locations where the thermoelectric current flows in and out the interface are labeled as r_0 and r_1 , respectively. A temperature gradient exists between r_0 and r_1 , where the corresponding temperatures are $T_0 < T_1$. The distance between r_0 and r_1 is defined as the characteristic length $\mathcal{L} = |r_1 - r_0|$. The direction of the current depends on the Seebeck coefficients of both materials, $S_{\mathcal{A}}$ and $S_{\mathcal{B}}$, following eq. (2.6).

2. Background

2.1. Thermoelectric Effects

Thermoelectric effects enable conversions between thermal and electric energy in electrically conducting materials. There are three different types: the Seebeck, Peltier, and Thomson effects (Terasaki 2011). The Peltier and Thomson effects in our experimental system produce temperature changes of order μK , which are not resolvable with our present thermometric capabilities. Moreover, such small temperature variations will not affect the dynamics of our system. Thus, Peltier and Thomson effects are not considered further.

The Seebeck effect describes the net spatial diffusion of electrons towards or away from a local temperature anomaly (Kasap 2001). As a consequence of this effect, positive and negative charges tend to become sequestered on opposite sides of a regional temperature gradient in the material, leading to the development of a thermoelectric electrical potential. Ohm's law then becomes (Shercliff 1979):

$$\mathbf{J} = \sigma (\mathbf{E} + \mathbf{u} \times \mathbf{B} - S \nabla T), \quad (2.1)$$

where $-\sigma S \nabla T$ encapsulates the thermoelectric current. The variables in eq. (2.1) are the electric current density \mathbf{J} , the electric conductivity σ ($\simeq 3.85 \times 10^6$ S/m in gallium), the electric field \mathbf{E} , the fluid velocity \mathbf{u} , the magnetic flux \mathbf{B} , the Seebeck coefficient S , and temperature T .

Mott & Jones (1958) derived the following expression for the Seebeck coefficient of a homogeneous and electrically conducting material as below:

$$S = -\frac{\pi^2 k_B^2 x_0}{3e E_{F0}} T, \quad (2.2)$$

where T is measured in Kelvin ($T \approx 300$ K for room temperature), $k_B = 1.38 \times 10^{-23}$ kg m²s⁻²K⁻¹ is the Boltzmann constant, x_0 is an $O(1)$ dimensionless constant that depends on the material properties, $e = 1.60 \times 10^{-19}$ C is the elementary electron charge, and E_{F0} is the material's Fermi energy (~ 10 eV = 1.6×10^{-18} J for metals). In a uniform medium, S is a function only of T . In this case, ∇S is parallel to ∇T such that $\nabla S \times \nabla T = 0$, which then requires that $S \nabla T$ is irrotational in a uniform medium.

As figure 1 shows, however, a temperature gradient at the interface of two materials with different Seebeck coefficients can generate a net thermoelectric potential. In this case, the Seebeck coefficient S discontinuously varies across the interface of the two

materials, \mathcal{A} and \mathcal{B} . Near r_0 and r_1 , ∇S is no longer parallel to ∇T , so a thermoelectric current can form a closed-looped circuit.

The thermoelectric potential, Φ_{TE} , can be calculated via the circuit integral

$$\Phi_{TE} = \oint \frac{\mathbf{J}_{TE} \cdot d\mathbf{r}}{\sigma_{AB}}, \quad (2.3)$$

where σ_{AB} is the effective electric conductivity of the two-material system. The effective electrical resistivity $\tilde{\rho}_{AB}$ is the sum of the resistivities in each material:

$$\tilde{\rho}_{AB} = \tilde{\rho}_A + \tilde{\rho}_B, \quad (2.4)$$

where we assume that the current travels through comparable cross-sectional areas and lengths in each material. Since $\sigma = 1/\tilde{\rho}$, the effective electrical conductivity for the thermoelectric circuit is

$$\sigma_{AB} = \frac{1}{\tilde{\rho}_{AB}} = \frac{1}{\tilde{\rho}_A + \tilde{\rho}_B} = \frac{\sigma_A \sigma_B}{\sigma_A + \sigma_B}. \quad (2.5)$$

Isolating the thermoelectric current density in the current loop, \mathbf{J}_{TE} , in eq. (2.1) yields

$$\mathbf{J}_{TE} = -\sigma_{AB} \tilde{S} \nabla T \approx -\sigma_{AB} \tilde{S} \left(\frac{T_1 - T_0}{\mathcal{L}} \right), \quad (2.6)$$

where \tilde{S} is the net Seebeck coefficient of the two-material system, and the temperature gradient in the $\hat{\mathbf{e}}_{\mathbf{n}}$ -direction is approximated by $(T_1 - T_0)/\mathcal{L}$ (see figure 1). Substituting eq. (2.6) into eq. (2.3), one can show that the net thermoelectric potential Φ_{TE} is the difference between the thermoelectric potentials in each material,

$$\Phi_{TE} = \Phi_A - \Phi_B = - \int_{r_0(T_0)}^{r_1(T_1)} S_A \nabla T \cdot d\mathbf{r} + \int_{r_0(T_0)}^{r_1(T_1)} S_B \nabla T \cdot d\mathbf{r}, \quad (2.7)$$

where r_0 and r_1 denotes the location where the thermoelectric current flows in and out the interface, and T_0 and T_1 are the temperatures at r_0 and r_1 , respectively. We set $T_0 < T_1$, so that the temperature gradient is positive from r_0 to r_1 , following figure 1. Here S_A and S_B are the Seebeck coefficients of materials \mathcal{A} and \mathcal{B} , respectively.

Substituting eq. (2.2) into eq. (2.7) then yields

$$\Phi_{TE} = \int_{r_0(T_0)}^{r_1(T_1)} (S_B - S_A) \nabla T \cdot d\mathbf{r} = \frac{\pi^2 k_B^2}{6e} \left[\frac{x_B}{E_{FB}} - \frac{x_A}{E_{FA}} \right] (T_1^2 - T_0^2), \quad (2.8)$$

where x_A , x_B , E_{FA} , and E_{FB} are numerical constants and Fermi energies of the materials \mathcal{A} and \mathcal{B} , respectively.

The system's *net Seebeck coefficient* is then written as

$$\tilde{S} = \frac{\Phi_{TE}}{T_1 - T_0} = \frac{\pi^2 k_B^2}{3e} \left[\frac{x_B}{E_{FB}} - \frac{x_A}{E_{FA}} \right] \left(\frac{T_0 + T_1}{2} \right), \quad (2.9)$$

where $(T_1 + T_0)/2$ is the mean temperature of the material interface. Note the structural similarity between the expressions for the Seebeck coefficient for a single material eq. (2.2) and the net Seebeck coefficient across a material interface eq. (2.9).

2.2. Governing Equations and Nondimensional Parameters

The magnetic Reynolds number, Rm , estimates the ratio of magnetic induction and diffusion in an MHD system. In our laboratory experiments, upper bounding values of Rm

are estimated by using the convective free-fall velocity (Julien *et al.* 1996; Glazier *et al.* 1999),

$$U_{ff} = \sqrt{\alpha_T \Delta T g H}, \quad (2.10)$$

leading to

$$Rm = \frac{U_{ff} H}{\eta} = Re Pm, \quad (2.11)$$

where Re is the Reynolds number, which denotes the ratio of inertial and viscous effects,

$$Re = \frac{U_{ff} H}{\nu}, \quad (2.12)$$

the magnetic Prandtl number is the ratio of the fluid's magnetic diffusivity η and its kinematic viscosity ν ,

$$Pm = \frac{\nu}{\eta}, \quad (2.13)$$

and α_T is the thermal expansivity of the fluid, ΔT is the vertical temperature difference across the fluid layer of depth H , g is the gravitational acceleration. In our experiments, $Re \lesssim 9 \times 10^3$ and $Pm \simeq 1.7 \times 10^{-6}$. Thus, $Rm \lesssim 0.015 \ll 1$ for our system, in good agreement with estimates made using ultrasonic velocity measurements in this same setup by Vogt *et al.* (2018a). Further, the free-fall timescale can be defined as

$$\tau_{ff} = H/U_{ff}. \quad (2.14)$$

The estimates above show that magnetic diffusion dominates induction in our experiments. In this low- Rm regime, the influence of fluid motions on the magnetic field can be neglected and the full magnetic induction equation need not be solved amongst the governing equations. This results in both Rm and Pm dropping out of the problem (Davidson 2016). This so-called ‘quasistatic approximation’ is commonly applied in low- Rm fluid systems and is valid in most laboratory and industrial liquid metal applications (e.g., Sarris *et al.* 2006; Davidson 2016; Knaepen & Moreau 2008).

In addition to quasistaticity, the Boussinesq approximation is applied (Oberbeck 1879; Boussinesq 1903; Gray & Giorgini 1976; Tritton 1977; Chillà & Schumacher 2012) and the governing equations of thermoelectric magnetoconvection (TEMC) are then

$$\mathbf{J} = \sigma (-\nabla\Phi + \mathbf{u} \times \mathbf{B} - S\nabla T), \quad (2.15a)$$

$$\nabla \cdot \mathbf{J} = 0, \quad (2.15b)$$

$$\frac{\partial \mathbf{u}}{\partial t} + (\mathbf{u} \cdot \nabla) \mathbf{u} = -\frac{1}{\rho} \nabla p + \frac{1}{\rho} (\mathbf{J} \times \mathbf{B}) + \nu \nabla^2 \mathbf{u} + \alpha_T \Delta T \mathbf{g}, \quad (2.15c)$$

$$\nabla \cdot \mathbf{u} = 0, \quad (2.15d)$$

$$\frac{\partial T}{\partial t} + (\mathbf{u} \cdot \nabla) T = \kappa \nabla^2 T, \quad (2.15e)$$

where ρ is fluid density, p is non-hydrostatic pressure, $\mathbf{g} = g\hat{\mathbf{e}}_z$ is the gravity vector, and κ is the thermal diffusivity. The external field is $\mathbf{B} = B\hat{\mathbf{e}}_b$. Note that Ohm's law (2.15a) has been simplified via the quasistatic approximation, such that the rotational part of electric field and perturbative second-order terms from $\mathbf{u} \times \mathbf{B}$ are not considered. Accordingly, in the bulk fluid, far from material interfaces, where net Seebeck effects

are small, the quasistatic Lorentz force is $\mathbf{J} \times \mathbf{B} \sim -\sigma \mathbf{u}_\perp B^2$, where \mathbf{u}_\perp is the velocity perpendicular to the direction of the magnetic field. Therefore, the low- Rm Lorentz force acts as a drag that opposes bulk fluid velocities that are directed perpendicular to \mathbf{B} (Sarris *et al.* 2006; Davidson 2016). This quasistatic Lorentz drag depends only on B^2 . In sharp contrast, the thermoelectric component of the Lorentz force, $-\sigma S \nabla T \times \mathbf{B}$, varies linearly with \mathbf{B} . Therefore, the thermoelectric Lorentz force changes sign when the direction of the applied magnetic field is flipped.

The dimensionless form of the TEMC governing equations are given in (A 1) and (A 2) in Appendix A. The nondimensional control groups in Appendix A may be decomposed into four parameters: the Prandtl number Pr , the Rayleigh number Ra , the Chandrasekhar number Ch , and the Seebeck number Se . The Prandtl number describes the thermo-mechanical properties of the fluid:

$$Pr = \frac{\nu}{\kappa}; \quad (2.16)$$

in liquid gallium, $Pr \approx 0.027$ at 40°C. The Rayleigh number characterizes the buoyancy forcing relative to thermoviscous damping:

$$Ra = \frac{\alpha_T \Delta T g H^3}{\nu \kappa}. \quad (2.17)$$

The Chandrasekhar number describes the ratio of quasistatic Lorentz and viscous forces:

$$Ch = \frac{\sigma B^2 H^2}{\rho \nu}. \quad (2.18)$$

The Seebeck number estimates the ratio of thermoelectric currents in the fluid and currents induced by fluid motions:

$$Se = \frac{|\tilde{S}| \Delta T / H}{U_{ff} B}. \quad (2.19)$$

Alternatively, Se can be cast as the ratio of the thermoelectrical potential and the motionally-induced potential in the fluid. Typical values of Se in our experiments with gallium-copper interfaces range from $O(10^{-2})$ to $O(1)$, implying that the Seebeck effect can generate dynamically significant experimental thermoelectric currents.

Lastly, the aspect ratio acts to describe the geometry of the fluid volume:

$$\Gamma = \frac{D}{H}, \quad (2.20)$$

where D is the inner diameter of the cylindrical container. We focus on $\Gamma = 2$ in this study, similar to Vogt *et al.* (2018a), and present only two $\Gamma = 1$ case results for contrast in Appendix C.

Alternatively, the groups of the above parameters that exist in (A 1) and (A 2) are the Péclet number Pe , the Reynolds number Re , the convective interaction parameter N_C and the thermoelectric interaction parameter $N_C Se$. The Péclet number,

$$Pe = \frac{U_{ff} H}{\kappa} = \sqrt{Ra Pr}, \quad (2.21)$$

estimates the ratio of thermal advection and thermal diffusion in the thermal energy equation. The convective interaction parameter N_C is the ratio of quasistatic Lorentz drag and fluid inertia. It is defined as:

$$N_C = \frac{\sigma B^2 H}{\rho U_{ff}} = Ch \sqrt{\frac{Pr}{Ra}} = \frac{Ch}{Re}. \quad (2.22)$$

Number Names	Symbol	Definition	Equivalence	Current Study
Magnetic Reynolds	Rm	$\frac{U_{ff}H}{\eta}$	$RePm$	$\lesssim 10^{-2}$
Magnetic Prandtl	Pm	$\frac{\nu}{\eta}$		1.7×10^{-6}
Prandtl	Pr	$\frac{\nu}{\kappa}$		2.7×10^{-2}
Rayleigh	Ra	$\frac{\alpha g \Delta T H^3}{\nu \kappa}$		$\sim 2 \times 10^6$
Chandrasekhar	Ch	$\frac{\sigma B^2 H^2}{\rho \nu}$		$[0, 8.4 \times 10^4]$
Seebeck	Se	$\frac{ \tilde{S} \Delta T / H}{U_{ff} B}$		$\sim [10^{-2}, 1]$
Aspect Ratio	Γ	$\frac{D}{H}$		2.0
Reynolds	Re	$\frac{U_{ff}H}{\nu}$	$\sqrt{\frac{Ra}{Pr}}$	$\lesssim 8.7 \times 10^3$
Péclet	Pe	$\frac{U_{ff}H}{\kappa}$	\sqrt{RaPr}	$\lesssim 2.2 \times 10^2$
Convective Interaction	N_C	$\frac{\sigma B^2 H}{\rho U_{ff}}$	$\sqrt{\frac{Ch^2 Pr}{Ra}} = \frac{Ch}{Re}$	$\lesssim 10$
Thermoelectric Interaction	N_{TE}	$\frac{\sigma B \tilde{S} \Delta T}{\rho U_{ff}^2}$	$Se N_C$	$\lesssim 10$

TABLE 1. Nondimensional parameters and parameter groups in thermoelectric magnetoconvection (TEMC). The low values of the top two parameters show that the current experiments fall within the quasistatic approximation. The next five are the base parameters used to describe most of the experimental cases. The next four parameters are alternative groupings that arise in the nondimensional version of eq. (2.15) given in Appendix A.

When $N_C \gtrsim 1$, the Lorentz force will tend to strongly damp buoyancy-driven convective turbulence. Lastly, the thermoelectric interaction parameter, N_{TE} is the product of the convective interaction parameter N_C and the Seebeck number Se . This parameter approximates the ratio between the thermoelectric Lorentz force and the fluid inertia, and is given by

$$N_{TE} = \frac{\sigma B |\tilde{S}| \Delta T}{\rho U_{ff}^2} = Se N_C. \quad (2.23)$$

Thus, when $Se \sim 1$, the thermoelectric forces can become comparable to the MHD drag, at least in the vicinity of the material interfaces where the thermoelectric currents are maximal.

All the nondimensional parameters and their estimated values for our study are summarized in Table 1.

2.3. Previous Studies of Turbulent Magnetoconvection

Despite its broad relevance to natural and industrial systems, magnetoconvection has not been studied in great detail relative to non-magnetic RBC (e.g., Ahlers *et al.* 2009) and rotating convection (e.g., Aurnou *et al.* 2015). Further, laboratory and numerical studies of turbulent MC have largely neglected thermoelectric effects to date (cf. Zhang *et al.* 2009). Thus, in reviewing the current state of turbulent MC studies, TE effects will not be considered.

In the limit of weak magnetic fields, such that $N_C \rightarrow 0$, turbulent MC behaves similarly to RBC (Cioni *et al.* 2000; Zürner *et al.* 2016), with the flow self-organizing into a large-scale circulation (LSC). Thus, the LSC is the base flow structure in turbulent MC when the dynamical effects of the magnetic field are subdominant (Zürner *et al.* 2020). LSCs, the largest turbulent overturning structure in the bulk fluid, have been studied extensively in RBC systems (e.g., Xia *et al.* 2003; Xi *et al.* 2004; Sun *et al.* 2005; Von Hardenberg *et al.* 2008; Brown & Ahlers 2009; Ahlers *et al.* 2009; Chillà & Schumacher 2012; Pandey *et al.* 2018; Stevens *et al.* 2018; Vogt *et al.* 2018a; Zürner *et al.* 2020).

Vogt *et al.* (2018a) carried out turbulent RBC laboratory (and associated numerical) experiments in a $\Gamma = 2$ liquid gallium cell using the same laboratory device as we employ in this study. Coupling the DNS outputs to laboratory thermo-velocimetric data, Vogt *et al.* (2018a) found that the turbulent liquid metal convection was dominated by a so-called jump rope vortex (JRV) LSC mode, instead of the sloshing and torsional modes found in the majority of $\Gamma = 1$ experiments (e.g., Funfschilling & Ahlers 2004; Funfschilling *et al.* 2008; Brown & Ahlers 2009; Xi *et al.* 2009; Zhou *et al.* 2009). The JRV had a characteristic oscillation frequency \tilde{f}_{JRV} of

$$\tilde{f}_{JRV} = f_{JRV}/f_\kappa = 0.027Ra^{0.419}, \quad (2.24)$$

where f_κ is the inverse of the thermal diffusion timescale

$$\tau_\kappa = H^2/\kappa. \quad (2.25)$$

Ultrasonic measurements yielded an LSC velocity scaling corresponding to

$$Re_{JRV} = 0.99 (Ra/Pr)^{0.483}, \quad (2.26)$$

formulated using their mean Prandtl number value, $Pr \simeq 0.027$. These velocity measurements approach the free-fall velocity scaling in which $Re = U_{ff}H/\nu = (Ra/Pr)^{1/2}$. Thus, we will use U_{ff} as the characteristic velocity scale when nondimensionalizing our equations in Appendix A and in the model of thermoelectric LSC precession developed in §6.

The quasistatic Lorentz force does, however, impede the convective motions in finite N_C cases. Zürner *et al.* (2020) used ultrasonic velocimetry measurements to develop an empirical scaling law for the global characteristic velocity, U_{MC} , in GaInSn MC experiments:

$$U_{MC} = \left(\frac{1}{1 + 0.68 N_C^{0.87}} \right) U_{ff}. \quad (2.27)$$

In §6, we will test both U_{MC} and U_{ff} in our model for thermoelectrical precession of the LSC, and show that the U_{MC} -based predictions better fit our precessional frequency measurements.

The turbulent LSC mode breaks down in MC when $N_C \gtrsim 1$ (Cioni *et al.* 2000; Zürner *et al.* 2019, 2020). This is roughly analogous to the loss of the LSC in rotating convection when the Rossby number is decreased below unity (Kunnen *et al.* 2008;

Horn & Shishkina 2015). In the supercritical $N_C \gtrsim 1$ regime, the convection in the fluid bulk should then become multi-cellular, akin to the flows shown in Yan *et al.* (2019).

Near the onset of the magnetoconvection, wall modes appear near the vertical boundaries and will become unstable before bulk convection in many geometrically-confined MC systems (Busse 2008).

It is important to stress that MC wall modes do not drift along the wall, in contrast to rotating convection (Ecke *et al.* 1992), since the quasistatic Lorentz force does not break azimuthal reflection symmetry (e.g., Houchens *et al.* 2002). The multi-cellular and magneto-wall mode regimes were both investigated in the numerical MC simulations of Liu *et al.* (2018). The wall modes were found not to drift in their large-aspect ratio simulations, similar to the experimental findings of Zürner *et al.* (2020). Further, Liu *et al.* (2018) showed that the wall modes could become unstable and inject nearly axially-invariant jets into the fluid bulk.

Strong wall mode injections are also found in the numerical MC simulations of Akhmedagaev *et al.* (2020). These injected axially-invariant jets are accompanied by a net azimuthal drift of the flow field, whose drift direction appears to be randomly set. We interpret these drifting flows as being controlled by the collisional interaction of the jets, qualitatively similar in nature to the onset of the shearing flows in the plane layer simulations of Goluskin *et al.* (2014). Therefore, we argue that the drifting effect found in the $N_C > 1$ near-onset numerical simulation by Akhmedagaev *et al.* (2020) fundamentally differs from the LSC precession found in the thermoelectrically-active $N_C \lesssim 1$ experiments reported herein.

3. Experimental Set-up and Methods

Laboratory MC experiments are conducted using UCLA's RoMag device, as shown in figure 2. See the appendix of King *et al.* (2012) for device details. Here, a vertical magnetic field is applied to an upright, non-rotating cylindrical tank filled with liquid gallium ($Pr \simeq 0.027$). The magnetic field vector is

$$\mathbf{B} = B\hat{\mathbf{e}}_{\mathbf{b}}, \quad \text{where} \quad \hat{\mathbf{e}}_{\mathbf{b}} = \pm\hat{\mathbf{e}}_{\mathbf{z}}, \quad (3.1)$$

such that $\hat{\mathbf{e}}_{\mathbf{b}} = +\hat{\mathbf{e}}_{\mathbf{z}}$ corresponds to an upward magnetic field vector and $\hat{\mathbf{e}}_{\mathbf{b}} = -\hat{\mathbf{e}}_{\mathbf{z}}$ corresponds to a downward magnetic field vector. The magnetic field is generated by an hourglass solenoid. With the tank centered along the bore of the solenoid, the vertical component of the magnetic field is constant over the fluid volume to within $\pm 0.5\%$ (King & Aurnou 2015). The magnetic field strength can be varied from 0 to 650 gauss, corresponding to a maximum Chandrasekhar value of $Ch = 8.4 \times 10^4$.

The material properties of liquid gallium are adapted from Aurnou *et al.* (2018). The container is made up of a cylindrical sidewall and a set of top and bottom end-blocks; the sidewall has an inner diameter $D = 2R = 196.8$ mm and the fluid layer height is fixed at $H = 98.4$ mm such that $\Gamma = 2.0$. We control the thermoelectric effects by changing the materials of these bounding elements. In specific, two different sets of boundaries are used. The first set is made up of an acrylic sidewall and Teflon coated aluminum end-blocks, in order to achieve electrically-insulated boundary conditions. The second set uses a stainless steel 316L sidewall and copper end-blocks, which provide electrically-conducting boundary conditions. The copper is uncoated and has been allowed to chemically interact with the gallium. This copper interface is not perfectly smooth due to gallium corrosion, allowing gallium to fully wets the surface. This is important as liquid metals often fail to make good surface contact with extremely smooth, pristine surfaces, likely due to strong surface tension effects.

The bottom of the convection stack is heated with a non-inductively wound electrical resistance pad (figure 2(c)), with the heating power held at a fixed value, P_{input} , in each experiment. Heat is extracted at the top of the convection stack by circulating thermostated cooling fluid through an aluminum heat exchanger that contains a double-spiral internal channel. Although the double wound channel minimizes the temperature gradients within the heat exchanger, the inlet and outlet ports must be at different temperatures due to the extraction of heat from the tank. The locations of the cooler inlet and warmer outlet are marked by arrows and triangles in figure 2(d), and in later figures just by the triangles.

By maintaining the time-mean difference between the horizontally averaged temperatures on the top and bottom boundaries, we are able to fix $Ra \approx 2 \times 10^6$ for all the experiments in this study. The sidewall of the tank is thermally insulated by a 5-cm thick Aspen Aerogels' Cryogel X201 blanket (not shown), which has a thermal conductivity of 0.015 W/(mK). The heating power lost from the sidewall and endwalls, P_{loss} , is estimated and then subtracted from the total input power, so that the effective heating power is $P = P_{input} - P_{loss}$.

Twelve thermistors are embedded in the top and bottom end-blocks roughly $\delta z = 2$ mm from the fluid-solid interface, and at cylindrical radius $r = 0.71R$. These are shown as the red probes in figure 2(d)). These thermistors are evenly separated 60° apart from each other in azimuth. Another six thermistors, shown in green in figure 2(d), are located on the exterior wall of the sidewall in the tank's midplane. The midplane thermistors are located at the same azimuth values as the top and bottom block thermistors, forming six vertically aligned thermistor triplets. Temperature data are simultaneously acquired at a rate of 10 Hz.

This thermometry data is discretized in both space and time. The discrete temperature time series data is expressed as

$$T_{ij}^k = T(\phi_i, t_j, z_k). \quad (3.2)$$

The index i ranges from 1 to 6, corresponding to the thermistor locations at 0° , 60° , 120° , 180° , 240° , and 300° azimuth, respectively. The time step in the data acquisition is denoted by the index j , which ranges from 1 to a final index value N for a given time series. Thermistor height is labeled via index $k = 1, 2$, or 3 , corresponding to the bottom block thermistors, the midplane thermistors and the top block thermistors, respectively. The bottom block thermistors are located at $z_1 = -2$ mm = 'bot'; the midplane thermistors are at $z_2 = 49.3$ mm = 'mid'; and the top block thermistors are set at $z_3 = 100.6$ mm = 'top'. No index is given for the radial position of the thermistors, so we reiterate that the end-block thermistors ($k = 1, 3$) are located at $r = 69.7$ mm = $0.71R$, whereas the midplane thermistors ($k = 2$) are on the exterior of the sidewall at $r = 100$ mm = $1.02R$.

The thermometry data is used to calculate the time-averaged temperature difference across the height of the fluid layer, ΔT , defined as

$$\Delta T = T^{bot} - T^{top}, \quad (3.3)$$

where T^{bot} and T^{top} are the time and azimuthal mean temperatures of the bottom and top end-block boundaries. These horizontal means are calculated via

$$T^{bot} = \frac{1}{6N} \sum_{i=1}^6 \sum_{j=1}^N T_{ij}^{bot} \quad \text{and} \quad T^{top} = \frac{1}{6N} \sum_{i=1}^6 \sum_{j=1}^N T_{ij}^{top}. \quad (3.4)$$

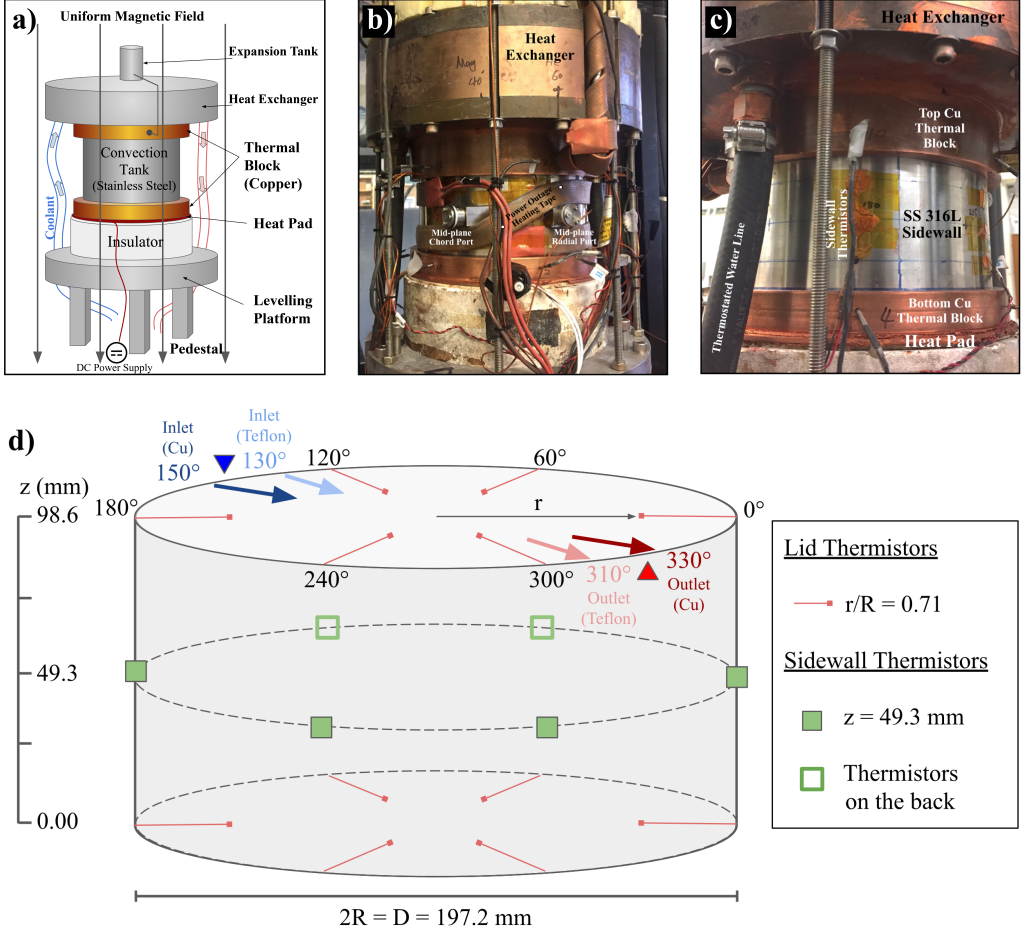


FIGURE 2. (a) Schematic of the laboratory apparatus. (b) Image of the convection tank with heat exchanger and safety heating tape in case of a power outage. (c) Closer in image of the sidewall and top and bottom thermal end-blocks. The device is thermally insulated by an aerogel blanket that is not shown here. (d) Schematic showing the top, bottom, and midplane thermistor placements. The sidewall midplane thermistors vertically align with the top and bottom thermistor locations. The top and bottom thermistors are located 2 mm from the fluid surfaces and extend horizontally 28.9 mm into the lids from the side. The blue and red arrows on the top mark the azimuth position of the inlet (cooler coolant) and outlet (warmer coolant) locations on the heat exchanger. In the following figures, these azimuthal angles are marked by the downward blue triangle and the upward red triangle.

This indexing convention will be used throughout this treatment. Further, T^k denotes the time-azimuthal mean temperature on the index k horizontal plane.

The material properties of the working fluid are determined using the mean temperature of the fluid volume

$$\bar{T} = (T^{bot} + T^{top}) / 2. \quad (3.5)$$

These, in turn, can then be used to measure the heat transfer efficiency of the system, characterized by the Nusselt number,

$$Nu = \frac{qH}{\lambda\Delta T}, \quad (3.6)$$

where $q = 4P/(\pi D^2)$ is the heat flux, and $\lambda = 31.4 \text{ W/(m K)}$ is the thermal conductivity of gallium. The Nusselt number describes the ratio of the total and conductive heat transfer across the fluid layer (e.g., Cheng & Aurnou 2016).

The physical properties of the boundary are also very important in this study. The isothermality of the bounding end-blocks is typically characterized by the Biot number,

$$Bi = \frac{Nu(\lambda/H)}{\lambda_s/D_s}, \quad (3.7)$$

where λ_s and D_s are the solid end-block's thermal conductivity and thickness, respectively. This parameter estimates the effective thermal conductance of the convective fluid layer to that of the solid bounding block. When $Bi \ll 1$, it is typically argued that boundary conditions are nearly isothermal, since the thermal conductance in the solid so greatly exceeds that of the fluid. We estimate $Bi = 0.07$ for the top copper lid and $Bi = 0.22$ for the bottom Cu end-block. A similar estimation suggests that $Bi = 0.24$ for both Teflon-coat aluminum boundaries. These Bi values would suggest that boundary thermal anomalies are approximately 10% of ΔT (e.g., Verzicco 2004).

This estimate, however, is not accurate in moderate Pe , low Pr liquid metal convection (Vogt *et al.* 2018a), where the convective flux is predominantly carried by large-scale inertial flows with thermal anomalies that approach ΔT . These large amplitude thermal anomalies tend to generate significant signals on the container boundaries.

Furthermore, in low to moderate Pe liquid metal convection, higher Nu implies larger interior temperature gradients since the convective heat flux is carried by large-scale, large amplitude temperature anomalies, instead of via small-scale turbulent plumes (e.g., Grossmann & Lohse 2004). These temperature anomalies imprint on the top and bottom boundaries and create non-isothermal interfacial conditions. We infer from our T_{ij}^k data that significant interfacial non-isothermality exists in our experiments and that these interfacial thermal anomalies can generate thermoelectric currents that drive long-period dynamics in our TE-MC cases at $0.1 \lesssim N_C \lesssim 1$.

4. Magnetoconvection with Electrically Insulating Boundaries

A baseline experiment is presented first in which the boundaries are electrically insulating. Aluminum end-blocks coated in Teflon ($\sigma \approx 10^{-24} \text{ S/m}$) are used in conjunction with an acrylic sidewall. The Rayleigh number is fixed at $Ra = 1.61 \times 10^6$ and the equilibrated experiment is run continuously for $t = 42.8 \tau_\kappa = 9.6 \times 10^3 \tau_{ff}$. During this 8.9-hour data acquisition, three separate sub-experiments are carried out. During the first $13.6 \tau_\kappa$, a 120 gauss downwardly directed ($\hat{\mathbf{e}}_b = -\hat{\mathbf{e}}_z$) magnetic field is applied, such that $Ch = 2.42 \times 10^3$, and $N_C = 0.31$. This sub-case is called *Insulating MC⁻*. The magnetic field is set to zero in the next sub-case, *Insulating RBC*, which extends from $t = 13.6 \tau_\kappa$ to $28.8 \tau_\kappa$. The 120 gauss magnetic field is turned back on, but its direction is flipped such that it is directed upwards ($\hat{\mathbf{e}}_b = +\hat{\mathbf{e}}_z$) in the last sub-case, *Insulating MC⁺*, which runs from $t = 28.8 \tau_\kappa$ to $42.8 \tau_\kappa$. The Nusselt number is approximately constant, $Nu \simeq 5.8$, in all three sub-cases. (See Table 4 for detailed parameter values.)

Figure 3 shows the temperature time series from the electrically-insulating experiment on a) the top end block T_{ij}^{top} , (b) the sidewall midplane T_{ij}^{mid} , and (c) the bottom end block T_{ij}^{bot} . The horizontal axis shows time normalized by the nondimensional thermal diffusion time t/τ_κ . In each panel, the line color represents an individual thermistor, each spaced 60 degrees apart in each layer (as shown in Figure 2).

The temperature time series in the midplane contains less high-frequency variance relative to the top and bottom block thermistor signals because the measurement is taken

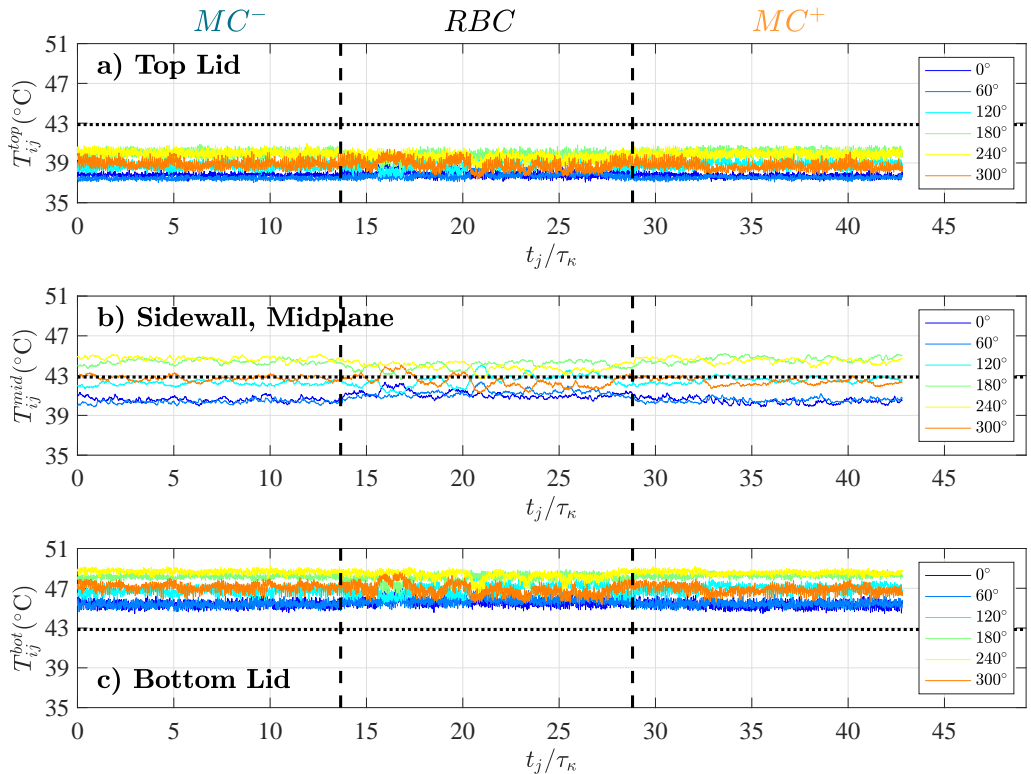


FIGURE 3. Temperature time series for the $Ra = 1.61 \times 10^6$, $Nu = 5.8$ electrically-insulated (Teflon) boundary conditions experiment. Data from thermistors, with locations shown in Figure 2d, embedded in the top boundary T_{ij}^{top} in (a); located on the exterior of the acrylic sidewall mid-plane T_{ij}^{mid} in (b); and embedded in the bottom boundary T_{ij}^{bot} in (c). The mean fluid temperature is $\bar{T} = 42.90^{\circ}C$, as marked by the horizontal dotted lines in each panel. The abscissa shows the time normalized by the thermal diffusion time scale t/τ_κ . This experiment contains three successive subcases that are divided by two dashed vertical lines: *Insulating MC^-* , *Insulating RBC* , and *Insulating MC^+* . No significant differences are found between the *Insulating MC^-* and *Insulating MC^+* cases, as is expected for non-thermoelectric, quasistatic magnetoconvection. See Table 4 for detailed parameter values.

outside the acrylic sidewall, and thus is damped by skin effects. The temperatures in the top block are all well below the mean temperature of the fluid (black dotted line); the midplane temperatures are adequately situated around the mean temperature line, and the bottom block temperatures are all well above the mean temperature. However, the temperature range in each panel covers nearly 50% of the mean temperature difference ΔT across the fluid layer. This implies strong horizontal temperature anomalies exist in the end blocks, even though the Biot numbers for this experiment is well below unity ($Bi \simeq 0.24$). The RBC case features slightly lower peak-to-peak temperature variations in the midplane thermistors, along with a slightly higher variance in each time series. This suggests that the RBC case carries more of the convective heat flux via higher speed, magnetically undamped flows with regards to the MC^- and MC^+ cases. Importantly for later comparisons to cases with electrically-conducting boundaries, the MC^- and MC^+ cases are essentially identical in all their statistical properties and behaviors. Thus, these two MC cases are not sensitive to the direction of \mathbf{B} , as is expected in quasi-static, non-thermoelectrically-active magnetoconvection.

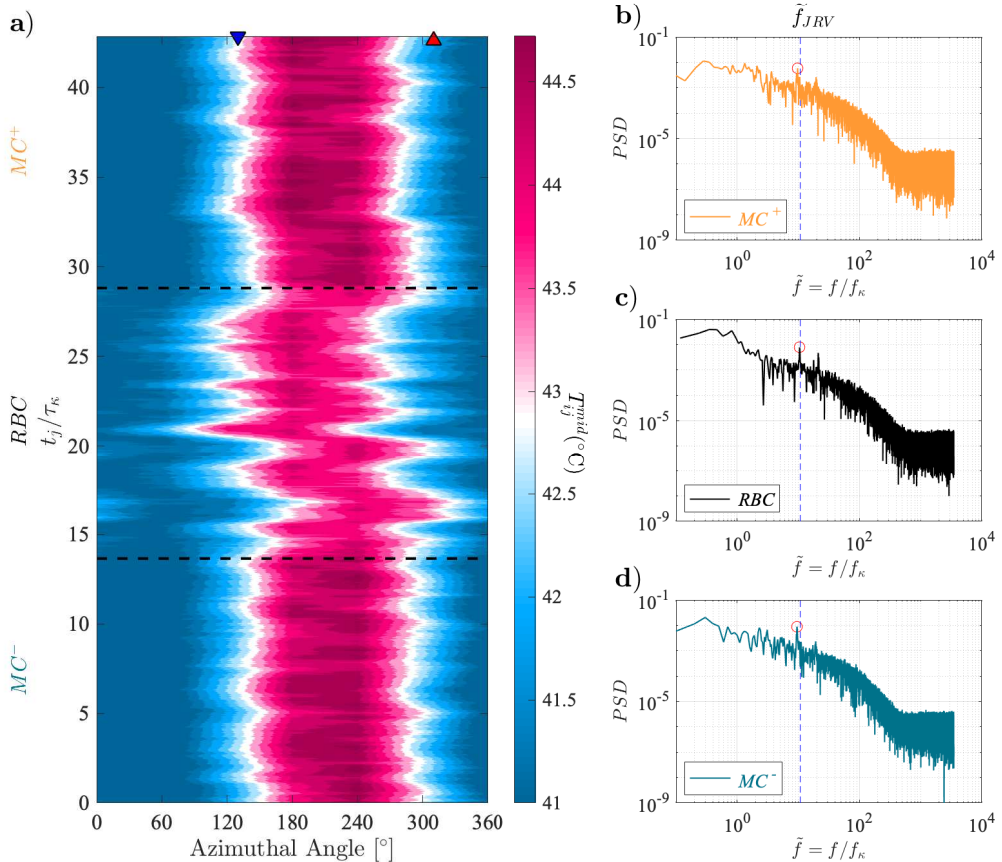


FIGURE 4. Electrically-insulating boundary study: (a) a contour map of the mid-plane sidewall temperature field T_{ij}^{mid} in the $Ra = 1.61 \times 10^6$ case (i.e., corresponding to fig. 3(b)). The horizontal axis shows the azimuthal angle around the tank; the vertical axis shows time normalized by τ_{κ} . The blue, downward (red, upward) triangle on the top axis denotes the azimuth of the heat exchanger inlet (outlet) location. The black dashed lines separate the *Insulating* MC^- , *Insulating* RBC and *Insulating* MC^+ subcases. Hann-windowed FFTs of the temperature data from the midplane thermistor located at 120° are shown for (b) the *Insulating* MC^+ subcase; (c) the *Insulating* RBC subcase; (d) the *Insulating* MC^- subcase. The red circles mark the lowest frequency sharp spectral peaks that correspond to the empirical characteristic frequency prediction for turbulent RBC , (Vogt *et al.* 2018a) $\tilde{f}_{JRV} = f_{JRV}/f_{\kappa} \approx 10.77$, shown as the blue dashed vertical lines in each spectrum. In the *Insulating* RBC case, the distinct sharp peak frequency normalized by the thermal diffusion frequency $f_{peak}/f_{\kappa} \approx 10.51$. This agrees within 2.5% with \tilde{f}_{JRV} .

Figure 4(a) shows the spatiotemporal evolution of the midplane temperature data T_{ij}^{mid} in the electrically insulating experiment. The colormap represents the temperature, in which red (blue) regions are hotter (colder) relative to the mean value (white). The midplane temperature field contains a warmer region on one side of the tank and a downwelling region antipodal to that, as found in RBC cases with a single LSC (e.g., Brown & Ahlers 2007; Vogt *et al.* 2018a; Zürner *et al.* 2019). Thus, we argue based on figure 4(a) that a turbulent LSC is present in these electrically-insulating boundaries

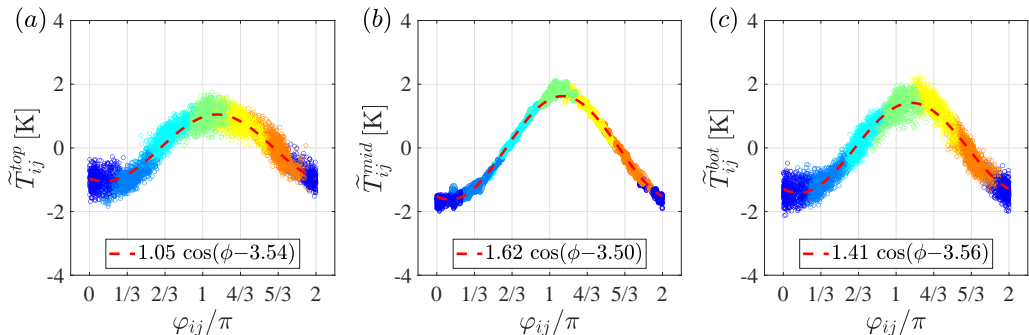


FIGURE 5. Temperature data of the *Insulating RBC* case shifted azimuthally into the best fit LSC frame, \tilde{T}_{ij}^k , in (a) the top block; (b) the sidewall midplane; and (c) the bottom block. The vertical axis is the temperature minus the azimuthal mean temperature at each time step. Different colors are used to label the location of the thermistors in the lab frames as the LSC fluctuates around its mean position following the color scale convention used in figure 3. The colors from left (blue) to right (orange) correspond to thermistors $i = 1$ to 6, respectively. The time-averaged best fit sinusoidal temperature profile is shown via the dashed red line in each panel.

$N_C \lesssim 1$ experiments, and that it maintains a nearly fixed azimuthal alignment for over $40 \tau_\kappa$.

Figures 4(b)-(d) show the spectral power density of the averaged temperature signals from each horizontal plane plotted versus normalized frequency, $\tilde{f} = f/f_\kappa$. The vertical dashed lines denote the normalized frequency predictions, \tilde{f}_{JRV} , for the jump rope LSC described in Vogt *et al.* (2018a). The lowest frequency sharp spectral peaks correspond to the JRV frequency and are marked with red circles, matching that of Vogt *et al.* (2018a) to within 2.5% in the *Insulating RBC* case. (The broad lower frequency peaks correspond to the slow meanderings of the LSC plane.) The distinct sharp peaks in both the *Insulating MC*⁺ and the *Insulating MC*⁻ FFTs are $\approx 25\%$ lower than \tilde{f}_{JRV} . We infer then, based on figure 4, that a quasi-stationary turbulent LSC flow is maintained in these electrically insulating, $N_C < 1$ experiments. The magnetic field does, however, cause a roughly 25% decrease in the LSC oscillation frequency, likely because magnetic drag reduces the characteristic flow speeds. This agrees adequately with eq. (2.27), which predicts a 20% decrease in flow speed at $N_C = 0.31$.

Following prior LSC studies (e.g., Cioni *et al.* 1997; Brown & Ahlers 2009; Xi *et al.* 2009; Zhou *et al.* 2009), we approximate the horizontal temperature profile as a sinusoid varying with azimuth angle ϕ at each point in the time series:

$$T_{fit}^k(t_j) = A_j^k \cos(\phi - \xi_j^k) + T_j^k. \quad (4.1)$$

On each z -level, A_j^k is the instantaneous amplitude of the sinusoidal temperature variation, ξ_j^k denotes the instantaneous azimuthal orientation of the LSC plane, and the instantaneous azimuthal-mean temperature is T_j^k . Using eq. (4.1), we best fit each z -level's temperature data at every time step.

Figure 5 shows the *insulating RBC* temperature anomaly on the top plane (a), mid-plane (b), and bottom planes (c), but with the data at each time step azimuthally-shifted into the best-fit LSC frame. This is accomplished by plotting \tilde{T}_{ij}^k , defined as

$$\tilde{T}_{ij}^k \equiv T_{ij}^k(\phi_{ij}^k, t_j) - T_j^k \quad \text{where} \quad \phi_{ij}^k \equiv \phi_{ij}^k - [\xi_j^k - \xi]. \quad (4.2)$$

The new azimuth variable ϕ_{ij}^k shifts each instantaneous thermistor measurement T_{ij}^k to

its azimuthal location relative to the best fit LSC azimuthal orientation angle ξ_j^k in eq. (4.1). The best fit LSC orientation angle averaged over time and over z -level is $\xi = 3.55$ rad for this case. The time-mean best fit sinusoid for the data on each z -level is plotted as a dashed red in each panel, with the best fit given in the legend box. The color of each thermistor follows the convention used in figure 3. The well-defined patches of color in figure 5 are aligned with the individual thermistor locations, producing a rainbow color pattern. The relative fixity of these color patches shows that the approximately sinusoidal temperature pattern does not drift significantly in time in this sub-case. Although they are not shown here, similar rainbow patterns also exist for the two insulating MC sub-cases.

In sum, we take figures 3 through 5 as evidence of a quasi-stationary, container-scale LSC in all three electrically insulating sub-cases made with $N_C \lesssim 0.3$.

5. Thermoelectric Magnetoconvection with Conducting Boundaries

Another approximately $48\tau_\kappa$ experiment has been carried out, but with all the boundaries electrically conducting such that thermoelectric effects can now affect the system, in contrast to the electrically insulating experiment presented in §4. The end-blocks used here are copper and the sidewall is stainless steel 316L. The heating power is fixed at 396.2W, leading to $Ra \simeq 1.8 \times 10^6$ and $Nu \simeq 5.9$. The experiment is made up of three successive sub-cases, *Conducting MC⁺*, *Conducting RBC*, and *Conducting MC⁻*, having an upward 120 gauss applied magnetic field $+\hat{e}_z$, no magnetic field, and then a downward 120 gauss magnetic field $-\hat{e}_z$, respectively. This corresponds to $N_C \simeq 0.3$ in the two MC sub-cases and $N_C = 0$ in the RBC case, similar to the prior insulating sub-cases. Figure 6 - 8 correspond to figure 3 - 5. The exact parameters are given in table 4 in Appendix D.

Figure 6 presents the T_{ij}^k thermistor time series data from this electrically conducting experiment, following the same plotting conventions as figure 3. The time series shows that the *Conducting RBC* sub-case generates a nearly stationary LSC structure, similar to the time series in figure 3. In the *Conducting MC⁺* and *Conducting MC⁻* cases, the temperature signals oscillate periodically around the mean temperature of the same layer height. Moreover, the oscillation of different heights are in phase at each azimuthal position. The temperature measurements indicate the presence of a container scale, coherent thermal structure that precesses in time.

Figure 7 follows the same plotting conventions as figure 4. Figure 7(a) shows a temperature contour map of the midplane sidewall thermistors, T_{ij}^{mid} for the electrically-conducting experiment. In the *Conducting RBC* case, the temperature pattern remains roughly fixed in place, similar to the insulating case. In contrast to this, the temperature field is found to coherently translate in the $-\hat{e}_\phi$ direction in the *Conducting MC⁺* sub-case and to translate in the $+\hat{e}_\phi$ direction in the *Conducting MC⁻* sub-case. However, at any instant in time, t_j , the azimuthal temperature pattern is similar to that of the LSC-like pattern found in the electrically-insulating experiment, with one warmer region and an antipodal cooler region.

Comparing figures 4(a) and 7(a) shows that the instantaneous LSC-like temperature pattern precesses around the container only in MC cases with electrically conducting boundaries. Further, the precession direction depends on the sign of the magnetic field, as cannot be the case for standard quasi-static MHD processes. Thus, we hypothesize that an LSC exists in these electrically-conducting sub-cases, and that thermoelectric current loops exist across the container's electrically conducting boundaries which drive the LSC

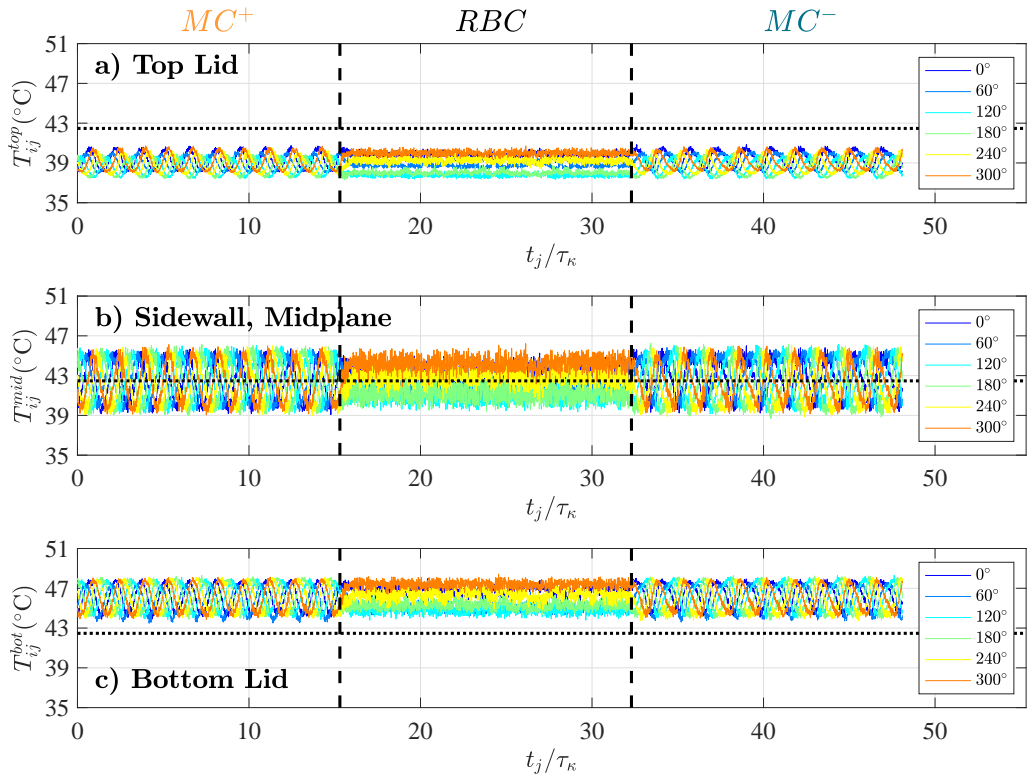


FIGURE 6. Temperature time series for the $Ra \simeq 1.82 \times 10^6$, $Nu \simeq 5.86$ electrically-conducting boundary conditions experiment. Data from thermistors, with locations shown in Figure 2d, embedded in the top boundary T_{ij}^{top} in (a); located on the exterior of the acrylic sidewall mid-plane T_{ij}^{mid} in (b); and embedded in the bottom boundary T_{ij}^{bot} in (c). The mean fluid temperature is $\bar{T} = 42.47^\circ\text{C}$, as marked by the horizontal dotted lines in each panel. The abscissa shows the time normalized by the thermal diffusion time scale t/τ_κ . This experiment contains three successive subcases that are divided by two dashed vertical lines: *Conducting* MC^- , *Conducting* RBC and *Conducting* MC^+ (Table 4). Large amplitude, low frequency thermal oscillations are observed at all thermistor locations in the *Conducting* MC^+ and *Conducting* MC^- subcases, which differs greatly with respect to the corresponding *Conducting* MC subcases in figure 3.

to precess azimuthally in time. Our model for this thermoelectric magnetoprecession (MP) process is presented in §6.

The figure 7(a) contour map also reveals that a slight asymmetry exists in the *Conducting* MC^- precession rate that does not exist in the *Conducting* MC^+ case. The precessional banding of the temperature field is uniform in the *Conducting* MC^+ case. In contrast, the bands have a slight variation in thickness in the *Conducting* MC^- case. We do not currently have an explanation for this difference between the MC^- and MC^+ cases.

Figures 7(b)-(d) show the time-averaged, thermal spectral power density plotted versus normalized frequency for the *Conducting* MC^+ , *Conducting* RBC , and *Conducting* MC^- sub-cases. To better identify the spectral peaks, these FFTs are made using three longer experimental cases, each up to $\approx 100\tau_\kappa$ in duration but employing the same control parameters. (Detailed parameter values are provided in Table 4.) The frequencies are normalized by the thermal diffusion frequency

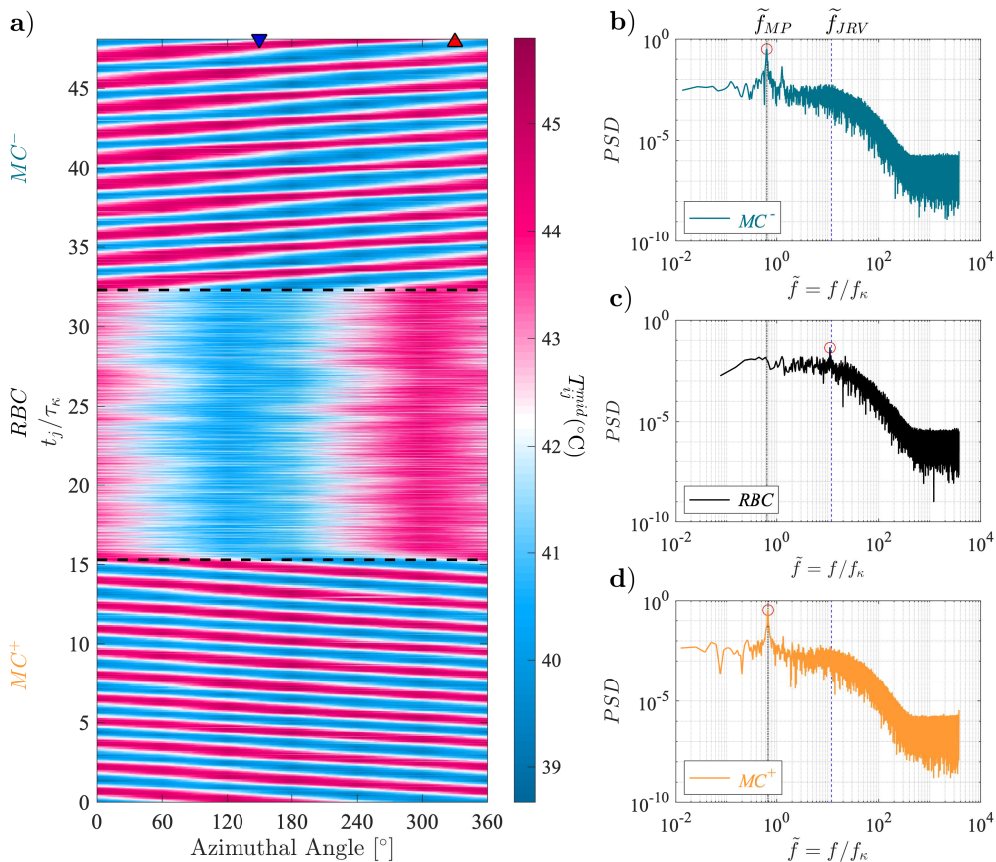


FIGURE 7. Identical to figure 4, but showing the $Ra \approx 1.8 \times 10^6$, $Nu \approx 5.8$ *Conducting* MC^+ , *Conducting* RBC , *Conducting* MC^- subcases experiment. However, all the FFTs here are analyzed using the *Long* version of the same experiments shown in appendix table 4. The averaged low frequency spectral peak in the *Conducting* MC subcases is marked by the vertical black dot-dashed lines in (b), (c) and (d). This corresponds to the magnetoprecessional (MP) mode and its nondimensional frequency is labeled \tilde{f}_{MP} .

$\tilde{f} = f/f_{\kappa} = f\tau_{\kappa}$. Red circles mark the peak frequency in each spectrum. The peak of the *Conducting* RBC sub-case is in good agreement with the predicted jump rope vortex frequency $f_{JRV} = 11.79$ (dashed blue vertical line). The magnetoprecessional frequency dominates the *Conducting* MC^- and *Conducting* MC^+ spectra in figures 7 (b) and (d), respectively. The peak frequencies are nearly identical in *Conducting* MC^- and *Conducting* MC^+ cases, with a mean value $\tilde{f}_{MP} = 0.66$ (black dot-dashed vertical line). Thus, magnetoprecession is slow relative to the jump rope mode, with $\tilde{f}_{MP} = 0.06\tilde{f}_{JRV}$.

Figure 8 is constructed parallel to figure 5, but plots the horizontal temperature anomalies of the *Conducting* MC^- thermistor data azimuthally-shifted into the best fit LSC reference frame. Since the LSC continually precesses in the $+\hat{e}_{\phi}$ direction in this sub-case, there is no mean location of the best fit LSC plane. For ease of comparison with figure 5, we set $\xi = 3.55$. In figure 5, each thermistor's data exists in an azimuthally-localized cloud since the LSC maintains its position over time. In

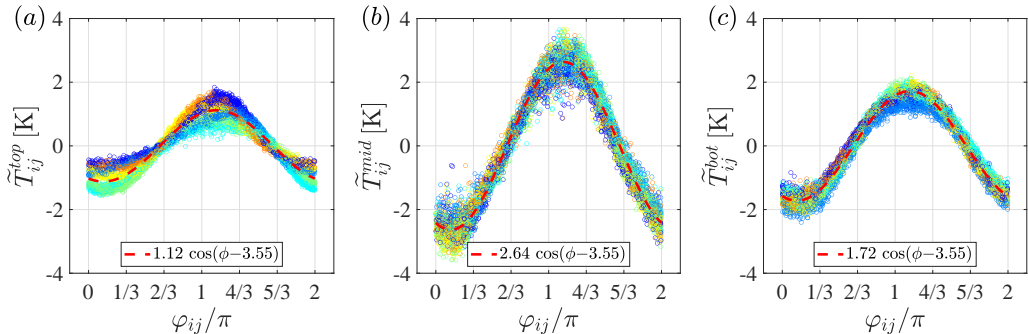


FIGURE 8. Temperature anomaly \tilde{T}_{ij}^k as defined eq. (4.2) on the a) top; b) midplane; and c) bottom horizontal planes in the LSC frame of the *Conducting MC⁻* subcase. For ease of comparison, we set $\xi = 3.55$, which is the same as the *Insulating RBC* case, since the precessing case does not have a meaningful time-averaged LSC position. The same colors are also used to label the location of the thermistors in the lab frames as figure 5. Contrary to figure 5, where the same color data cluster near a fixed azimuth, here each color is spread out and covers the entire azimuth relative to the LSC plane, which occurs because the LSC plane is constantly precessing through all the azimuthal angles. Panels (a) – (c) show that a sinusoidal temperature profile exists at each horizontal level k , with the largest amplitude in the midplane. The time-averaged best fit sinusoidal temperature profile is shown via the dashed red line in each panel.

contrast, each thermistor’s data points form an approximately continuous sinusoid in this magnetoprecessional case. This occurs since the thermal field precesses past each of the spatially fixed thermistors and, thus, each thermistor samples every part of the sinusoidally precessing temperature field over time.

The top block thermistor data sets in figure 8(a) deviate from that of a sinusoid. This is caused by spatially fixed $\simeq 0.5$ K temperature anomalies in the top block that are co-located with the inlet and outlet positions of the top block heat exchanger’s cooling loop, which are located at $\phi = 150^\circ$ and 330° , respectively. These fixed temperature anomalies are likely not evident in figure 5 because the orientation angle of the LSC remains nearly aligned with the heat exchanger inlet and outlet angles in the electrically-insulating experiment. In addition, we note that the midplane has a larger temperature variation in figure 8(b) than in the corresponding *Insulating RBC* case. This may be due to differences in Bi for the differing experiments.

5.1. Fixed $Ra \approx 2 \times 10^6$ TEMC Survey

To characterize the system’s behavioral regimes, we have conducted a survey of turbulent TEMC with the Rayleigh number fixed at approximately 2×10^6 and the Chandrasekhar number varying from 0 to 8×10^5 all with a vertically downward applied magnetic field ($\hat{\mathbf{e}}_{\mathbf{b}} = -\hat{\mathbf{e}}_{\mathbf{z}}$). Three regimes are found: (i) the jump rope vortex (*JRV*) regime; (ii) the magnetoprecessional (*MP*) regime; and (iii) the multi-cellular magnetoconvection (*MCMC*) regime.

Figure 9(a) shows a thermal spectrogram made using the T_{ij}^{mid} data, plotted as functions of f/f_κ on the vertical axis and the Chandrasekhar number Ch on the horizontal axis. Here, we use $Pr = 0.027$, and the RBC case’s $Ra_0 = 2.12 \times 10^6$ value to calculate N_C for all the cases. The peak frequency at each Ch -value is marked by an open black circle. Starting from the left of the figure, the predicted peak RBC frequency, \tilde{f}_{JRV} derived from equation eq. (2.24), is marked by the white, horizontal dashed line. In the JRV regime, the $0 < N_C \lesssim 10^{-1}$ experimental data are in good agreement with \tilde{f}_{JRV} , with sidewall thermal fields that correspond to that of an LSC-like flow (e.g., figure

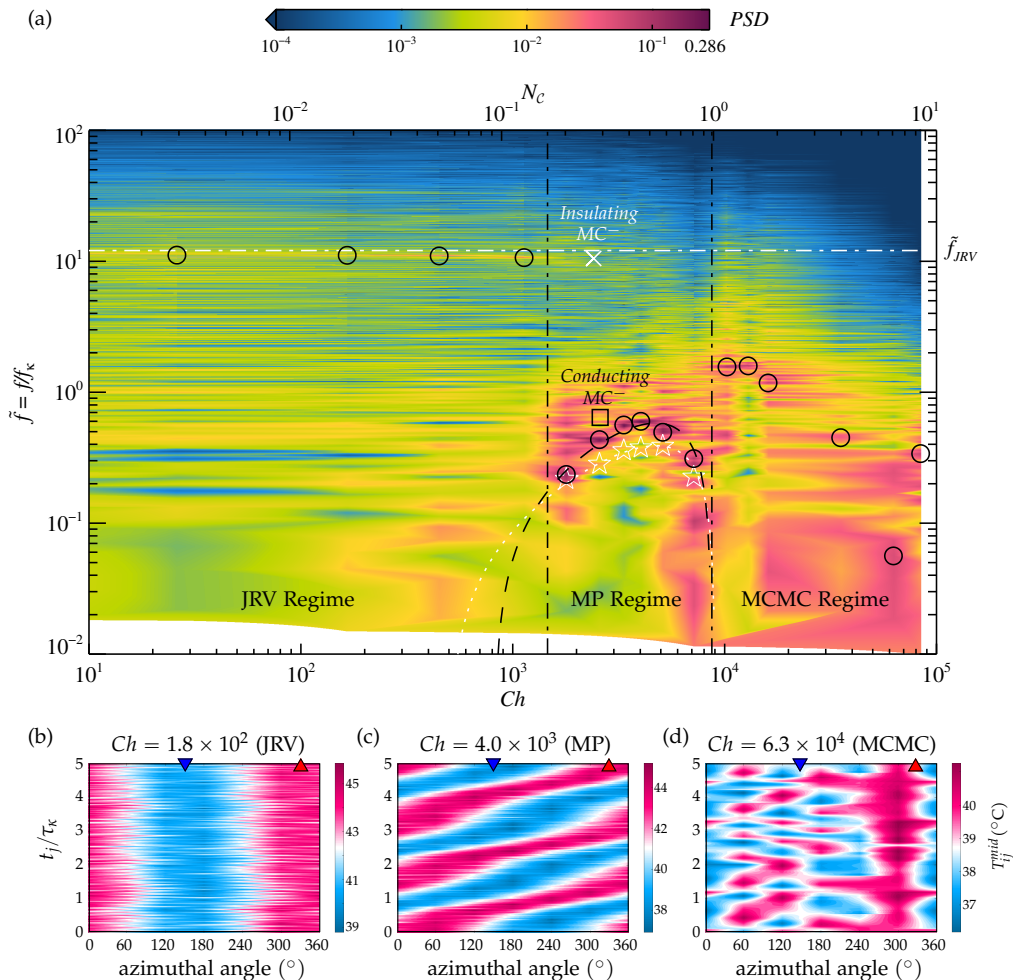


FIGURE 9. (a) Power spectral density (PSD) of the T_{ij}^{mid} temperature data versus Ch and N_C for the $Ra \approx 2 \times 10^6$ cases shown in table 5. The vertical axis is thermal diffusion frequency $\tilde{f} = f/f_\kappa$. The peak frequency for each case is marked with black open circles. The interaction parameter is calculated here as $N_C = \sqrt{Ch^2 Pr/Ra_0}$, where $Ra_0 = 2.12 \times 10^6$ corresponds to the case with no magnetic field. The jump rope vortex (JRV), the magnetoprecession (MP), and the multi-cellular magnetoconvection (MCMC) regimes are separated by the two black vertical dot-dashed lines. The JRV frequency (Vogt *et al.* 2018a), \tilde{f}_{JRV} , is shown as the white horizontal dotted line near $\tilde{f} \approx 12.1$. The black square marks the peak frequency of the *Conducting* MC^- case, and the white cross marks the peak frequency of the *Insulating* MC^- case. The black dashed curve denotes the second-order fit to the experimental data in the MP regime. The white stars are magnetoprecession frequency estimates calculated using eq. (6.20) for each MP case, and the white dotted curve is the second-order fit of these theoretical estimates developed in §6.5. The lower panels show sidewall midplane temperature contour maps in (b) JRV, (c) MP, and (d) MCMC regimes. The blue downwards and red upwards triangles in the lower panels denote the heat exchanger inlet and outlet azimuthal locations, respectively.

9(b)). In this regime, buoyancy-driven inertia is the dominant forcing in the system. As N_C increases and exceeds unity, it is expected that the LSC will weaken and eventually disappear (e.g., Cioni *et al.* 2000; Zürner *et al.* 2020). However, the MP regime exists in the intermediate N_C TEMC system. In this regime, the spectral peak switches from near to \tilde{f}_{JRV} to the slow magnetoprecessional frequency above $N_C \approx 0.1$, corresponding to the magnetoprecessional sidewall thermal signal shown in figure 9(c)). The MP frequency grows with N_C , reaching a value of $0.60 f_\kappa$ near $N_C \approx 0.4$. At higher N_C , the peak frequency decays, becomes unstable, and mixes with other complex modes at $N_C \gtrsim 1$ (e.g., figure 9(d)). The single, turbulent LSC likely gives way to multi-cellular bulk flow in this $N_C \gtrsim 1$ MCMC regime.

We contend that it is the existence of coherent thermoelectric current loops existing across the top and bottom horizontal interfaces of the fluid layer that drive the magnetoprecessional mode observed in the MP regime. Following the arguments of §2.1, this requires horizontal temperature gradients to exist along on these bounding interfaces as shown schematically in figure 1. To quantify this, the horizontal temperature difference at height z_k and time t_j is estimated using the best fit of the data to eq. (4.1) as

$$\delta T_j^k = \max(T_{fit}^k(t_j)) - \min(T_{fit}^k(t_j)) = 2A_j^k. \quad (5.1)$$

Its time-mean value is denoted by

$$\delta T^k = \frac{2}{N} \sum_{j=1}^N A_j^k, \quad (5.2)$$

where j is the j^{th} step in the discrete temperature time series and N is the total number of time steps. Thus, δT^{top} estimates the time-averaged, maximum horizontal temperature difference in the top block thermistors located at $z = 100.6 \text{ mm} = 1.022H$ and $r = 0.71R$. Similarly, δT^{bot} estimates this value using the bottom block thermistors located at $z = -2.0 \text{ mm} = -0.020H$ and $r = 0.71R$.

Figure 10(a) shows time series of the maximum *horizontal* temperature variations in the top and bottom boundaries in the reference frame of the fitted LSC plane, δT_j^k , calculated using eq. (5.1). This data is from our canonical *Conducting MC*⁻ case at $Ra = 1.83 \times 10^6$, $Ch = 2.59 \times 10^3$, and $N_C = 0.31$. The temperature time series for this case has been shown in figure 6. In the top block, the time-averaged maximum horizontal temperature variation, plotted in blue, is 2.24 K, which is 1.2 K smaller than that of the bottom block (in red), 3.44 K. Moreover, the top has a larger magnitude of fluctuation of ~ 2 K, while the bottom remains relatively stable with a fluctuation of ~ 1 K. The difference in top and bottom δT_j^k fluctuation amplitudes is likely due to the structure of the heat exchanger, in which the inlet and the outlet of the cooling water are antipodal to one another. This imposes a small (~ 1 K), spatially fixed temperature gradient along the line connecting these two points. This causes the horizontal temperature variation at the top boundary to fluctuate as the LSC precesses across the top block's spatially fixed temperature gradient. We hypothesize that this fluctuation propagates to the bottom boundary, generating a smaller fluctuation there than on the top block and lagging the top fluctuation by about 0.6 thermal diffusion times.

Figure 10(b) shows δT^k , the time-mean horizontal temperature differences calculated via eq. (5.2) on the top block (blue triangles) and on the bottom block (red triangles) for the $N_C < 1$ experiments in the fixed Ra survey ($Ra \approx 2 \times 10^6$). The *Conducting MC*⁻ case in panel (a) corresponds to the square markers on the right in panel (b). The horizontal dashed and dotted lines show the mean values of δT^k for the *Conducting MC*⁻ case. The two vertical dot-dashed lines denote the boundaries between the JRV, MP and

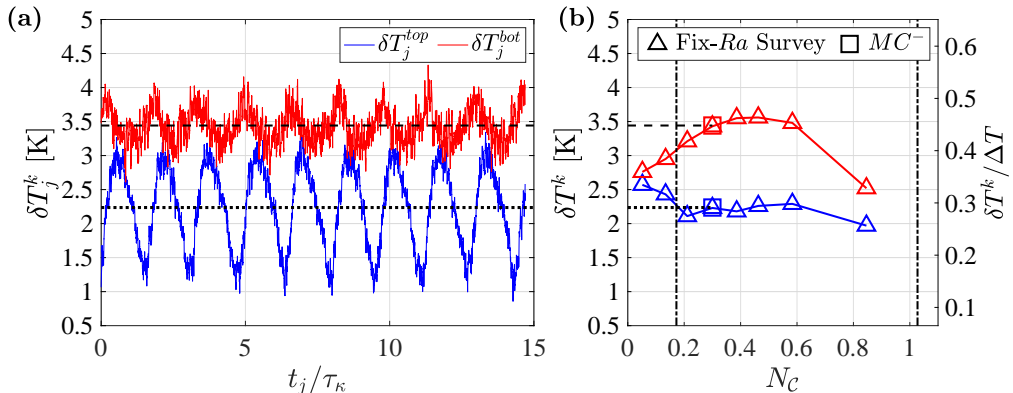


FIGURE 10. (a) Time series of the horizontal temperature difference at different heights δT_j^k , defined in eq. (5.1), from the *Conducting* MC^- case at $Ra = 1.83 \times 10^6$, $Ch = 2.59 \times 10^3$, and $N_C = 0.31$. The horizontal axis is normalized time t_j/τ_κ . The black dotted line denotes the mean values of $\delta T_j^{top} = 2.24$ K, and the black dashed line denotes $\delta T_j^{bot} = 3.44$ K. (b) Time-averaged horizontal temperature difference estimates δT_j^k on the top and bottom boundaries for the fixed- Ra cases ($Ra \approx 2 \times 10^6$) at $N_C < 1$. The fixed- Ra cases are marked by triangles; blue (red) color represents top (bottom) boundary measurements. The magnetoprecessional (MP) regime lies between the two vertical dot-dashed lines. The right hand y -axis denotes δT_j^k normalized by the averaged vertical temperature difference $\Delta T = 7.68$ K of the fixed- Ra cases shown here. Values of δT_j^k for the *Conducting* MC^- case are marked by the square symbols.

MCMC regimes. In the lowest N_C case shown in figure 10(b), it is found that $\delta T_j^{top} \approx \delta T_j^{bot} \approx 2.6$ K. This value is nearly 40% of the vertical temperature gradient across the tank, and is similar to values found for comparable RBC cases. We argue that this 2.6 K value is predominantly generated by the jump rope vortex imprinting its thermal anomalies onto the top and bottom boundary thermistors. The values of δT_j^{bot} exceed δT_j^{top} in the MP regime ($0.1 \lesssim N_C \lesssim 1$). For $N_C \gtrsim 1$, the jump rope-style LSC breaks down into multi-cellular flow (e.g., Zürner *et al.* 2020) and it is not possible to fit a sinusoidal function of the form (4.1) to the thermistor data in the top and bottom blocks.

The right hand vertical axis in figure 10(b) shows thermal block temperature differences normalized by the vertical temperature difference, $\delta T_j^k / \Delta T$. The fixed Ra survey cases have $\delta T_j^k / \Delta T$ values ranging from roughly 0.3 to 0.5, demonstrating that low Pr convective heat transfer occurs via large-scale, large amplitude thermal anomalies that may alter the thermal boundary conditions in finite Bi experiments. Such conditions differ from those typically assumed in theoretical models of low Prandtl number convection (e.g., Clever & Busse 1981; Thual 1992).

The slow magnetoprecessional modes only appear in MC experiments with electrically conducting boundaries for $0.1 \lesssim N_C \lesssim 1$. Strong, coherent horizontal temperature gradients exist along the top and bottom boundaries in these cases, as shown in figure 10. This suggests that magnetoprecession is controlled by the material properties of the boundaries and the horizontal temperature gradients on the liquid-solid interfaces. Based on these arguments, we develop a simple model for thermoelectrically-driven magnetoprecession of the LSC in the following section.

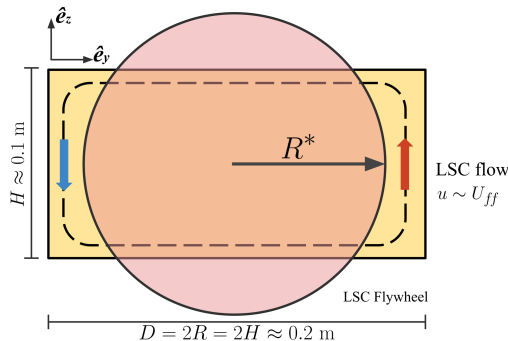


FIGURE 11. Cross-section view of the precessional flywheel model (pink) in the LSC plane (yellow). The precessional flywheel is assumed to have the same cross-sectional area as the LSC plane, $\pi(R^*)^2 = 2H^2$. The angular velocity of the overturning LSC flywheel is estimated by assuming it rotates at the free-fall speed $\omega_{LSC} \approx U_{ff}/R^*$.

6. Thermoelectric Precession Model

This study presents the first detailed characterization of the large-scale, long-period magnetoprecessional (MP) mode that appears in turbulent MC cases with conducting boundaries. We hypothesize that the MP mode emerges from an imbalance between the thermoelectric Lorentz forces at the top and bottom boundaries of the fluid layer. This imbalance, which arises due to the differing thermal gradients on the top and bottom boundaries, creates a net torque on the overturning LSC. This net torque causes the LSC to precess like a spinning top. To test this hypothesis, a simple mechanistic model of such a thermoelectrically-driven magnetoprecessing LSC is developed, and is shown to be capable of predicting the essential behaviors in our MP system.

6.1. Angular Momentum of the LSC Flywheel

A Cartesian coordinate frame is used in our model of thermoelectrically-driven magnetoprecession of the LSC. This Cartesian frame is fixed in the LSC plane such that \hat{e}_y always points along the $\xi_j = 0$ direction. The thermal gradient is also aligned in the same direction, yielding $\hat{e}_n = \hat{e}_y$. The magnetic field direction is oriented in $\pm\hat{e}_z$, and the right-handed normal to the LSC plane is oriented in the \hat{e}_x -direction.

We treat the LSC as a solid cylindrical flywheel that spins around a midplane \hat{e}_x -axis, as shown in figure 11. The LSC is taken to have the same cross-sectional area as the LSC plane, $A_{LSC} = \Gamma H^2$. The corresponding radius of the solid LSC cylinder is then

$$R^* = \sqrt{A_{LSC}/\pi} = \sqrt{\Gamma H^2/\pi}. \quad (6.1)$$

which corresponds to $R^* \approx 0.8H$ for the $\Gamma = 2$ experiments carried out here. The volume of the turbulent LSC is V_{LSC} . For convenience, we take the depth of the LSC in \hat{e}_x to be R^* so that $V_{LSC} = \pi R^{*3}$, noting that the assumed depth and V_{LSC} both drop out of our eventual prediction for the LSC's magnetoprecession rate ω_{MP} . The LSC flywheel, as constructed, does not physically fit within the tank since $R^* > H/2$, as shown in figure 11. (It is not shown to scale in figure 13(b).)

The angular momentum of the flywheel is taken to be that of a uniform-density solid cylinder with mass $M_{LSC} = \rho V_{LSC}$ and radius R^* , rotating around \hat{e}_x . Its moment of inertia with respect to the \hat{e}_x -axis is

$$I = \frac{1}{2}M_{LSC}R^{*2} = \frac{1}{2}\rho V_{LSC}R^{*2}. \quad (6.2)$$

We use the upper bounding free-fall velocity as an estimate of the angular velocity vector for the LSC flywheel:

$$\boldsymbol{\omega}_{LSC} \approx U_{ff}/R^* \hat{\mathbf{e}}_{\mathbf{x}}. \quad (6.3)$$

Thus, the angular momentum due to the overturning of the flywheel, \mathbf{L}_{LSC} , is oriented along $\hat{\mathbf{e}}_{\mathbf{x}}$ and is estimated as:

$$\mathbf{L}_{LSC} = I\boldsymbol{\omega}_{LSC} \approx \left(\frac{1}{2}\rho V_{LSC}R^{*2}\right) \left(\frac{U_{ff}}{R^*}\right) \hat{\mathbf{e}}_{\mathbf{x}} = \frac{1}{2}\rho V_{LSC}U_{ff}R^* \hat{\mathbf{e}}_{\mathbf{x}}. \quad (6.4)$$

6.2. Thermoelectric Currents at the Electrically Conducting Boundaries

Figure 12(a) shows a schematicized vertical slice through our experimental tank in the low N_C regime. The LSC generates horizontal thermal gradients on both horizontal boundaries. Thus, the end-blocks have a higher temperature near the upwelling branch of the LSC, which carries warmer fluid upwards, and the end-blocks are cooler near the downwelling branch of the LSC, which carries cooler fluid downwards. These temperature gradients on the top and bottom fluid-solid interfaces generate thermoelectric current loops. Eq. (2.7) is used to calculate the net Seebeck coefficient of such a thermoelectric current loop in our Cu-Ga system:

$$\Phi_{TE} = \int_{r_0(T_0)}^{r_1(T_1)} (S_{Cu} - S_{Ga}) \nabla T \cdot d\mathbf{r} = \frac{\pi^2 k_B^2}{6e} \left[\frac{x_{Cu}}{E_{FCu}} - \frac{x_{Ga}}{E_{FGa}} \right] (T_1^2 - T_0^2), \quad (6.5)$$

where S_{Ga} and S_{Cu} are Seebeck coefficients for gallium and copper, respectively, calculated via eq. (2.2). For gallium, the numeric coefficient x_0 is $x_{Ga} = 0.7$ (Cusack 1963) and the Fermi energy is $E_{FGa} = 10.37$ eV (Kasap 2001). For copper, $x_{Cu} = -1.79$ and $E_{FCu} = 7.01$ eV. The temperatures T_0 and T_1 represent the minimum and maximum temperatures, respectively, in a given horizontal plane (e.g., figure 1).

Following eq. (2.9), the net Seebeck coefficient on the k -level Cu-Ga interface is:

$$\tilde{S}^k = \frac{\pi^2 k_B^2}{3e} \left[\frac{x_{Cu}}{E_{FCu}} - \frac{x_{Ga}}{E_{FGa}} \right] T^k \equiv X_0 T^k \text{ [V/K]}, \quad (6.6)$$

where T^k is the time-azimuthal mean temperature on the k -interface. The Cu-Ga Seebeck prefactor X_0 collects all the constant and material properties in eq. (6.6). Its value in our system is

$$X_0 \approx -7.89 \times 10^{-9} \text{ V/K}^2. \quad (6.7)$$

Unlike the net Seebeck coefficient, X_0 does not depend on temperature.

The thermoelectric current density vector in liquid gallium is approximated via eq. (2.6):

$$\mathbf{J}_{TE}^k \approx \sigma_0 X_0 T^k \left(\frac{\delta T^k}{\mathcal{L}} \right) \hat{\mathbf{e}}_{\mathbf{y}}, \quad (6.8)$$

where $\sigma_0 = 3.63 \times 10^6$ S/m is the effective electric conductivity for the Cu-Ga system, calculated by substituting the conductivity of gallium ($\sigma_{Ga} \approx 3.88 \times 10^6$ S/m) and copper ($\sigma_{Cu} \approx 5.94 \times 10^7$ S/m) into eq. (2.5). The horizontal temperature gradient is approximated by the maximum temperature difference across the k -interface, δT^k , divided by a characteristic width of the current loop, \mathcal{L} . We assume this width is the same as the diameter D of the tank, $\mathcal{L} \approx \Gamma H = 2H = 197.2$ mm. (Effects of possible TE currents in the stainless steel sidewall ($\sigma_{St.Stl.} \approx 1.4 \times 10^6$ S/m) are not accounted for here.)

Figure 12(b) shows a circuit diagram for the thermoelectric current loop near the

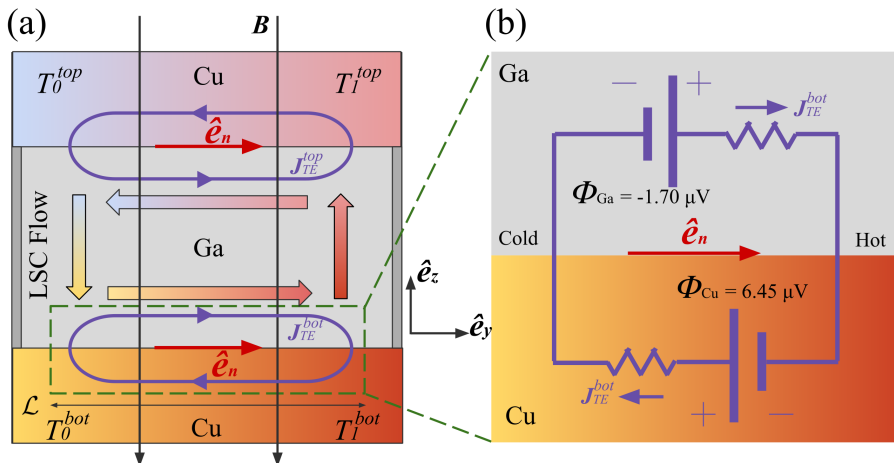


FIGURE 12. (a) Cross-sectional schematics of the experimental MC system with electrically conducting boundaries. In the plane of LSC, the turbulent LSC imprints large scale thermal anomalies onto the boundaries: the top boundary has a minimum temperature T_0^{top} and a maximum temperature T_1^{top} ; the bottom boundary has a minimum temperature T_0^{bot} and a maximum temperature T_1^{bot} . Thermoelectric potentials are generated at the Cu-Ga interfaces and form current density loops across the boundaries, \mathbf{J}_{TE}^{top} and \mathbf{J}_{TE}^{bot} , with a width of $\mathcal{L} \approx \Gamma H$. (b) Circuit diagram of the Cu-Ga system at the bottom boundary. The thermoelectric potential in gallium is denoted as Φ_{Ga} , which is smaller in magnitude and has an opposite sign as the thermoelectric potential in copper, Φ_{Cu} . Thus, the thermoelectric current flows from cold to hot in liquid gallium (in $+\hat{\mathbf{e}}_n$), and from hot to cold in copper (in $-\hat{\mathbf{e}}_n$).

experiment's bottom liquid-solid interface at $\approx 40^\circ\text{C}$. The thermoelectric potential in gallium has a negative sign, so the currents within the fluid are always aligned in the direction of the thermal gradient $\hat{\mathbf{e}}_n = \hat{\mathbf{e}}_y$. In contrast, the thermoelectric potential in copper has a positive sign, so the current flows from the hot to the cold region in $-\hat{\mathbf{e}}_n$.

6.3. Thermoelectric Forces and Torques

The thermoelectric component of the mean Lorentz forces density on the index k horizontal interface can be calculated, using eq. (6.8), as

$$\mathbf{f}_{TE}^k = \mathbf{J}_{TE}^k \times \mathbf{B} = \sigma_0 X_0 T^k \left(\frac{\delta T^k}{\Gamma H} \hat{\mathbf{e}}_y \right) \times B \hat{\mathbf{e}}_b = \frac{\sigma_0 X_0 B T^k \delta T^k}{\Gamma H} (\hat{\mathbf{e}}_y \times \hat{\mathbf{e}}_b), \quad (6.9)$$

where we have taken $\mathcal{L} \approx \Gamma H$. Since the thermoelectric currents are predominantly in the LSC plane and are aligned parallel to the thermal gradient, the thermoelectric Lorentz forces point in the $+\hat{\mathbf{e}}_x$ -direction for upward directed \mathbf{B} , and in the $-\hat{\mathbf{e}}_x$ -direction for downward directed \mathbf{B} (corresponding to figure 13(a)).

The Lorentz force is the volume integral of the force density:

$$\mathbf{F}_{TE}^k = \int \mathbf{f}_{TE}^k dV = \int \mathbf{J}_{TE}^k \times \mathbf{B} dV. \quad (6.10)$$

We coarsely assume that each thermoelectric current loop exists in the top half or bottom half of the LSC, and generates uniform Lorentz forces that act, respectively, on the upper or lower half of the LSC. With these assumptions, we take each hemicylindrical integration volume to be $V_{LSC}/2$. The Lorentz forces due to thermoelectric currents

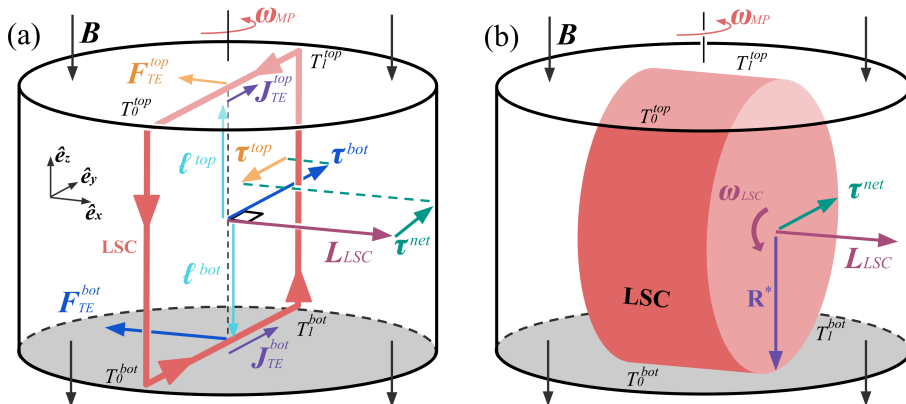


FIGURE 13. (a) Free-body diagram of thermoelectric LSC precession. The red arrows enclosed inside the tank represents the LSC. The thermoelectric potentials generate current in the liquid gallium at top and bottom boundaries: \mathbf{J}_{TE}^{top} and \mathbf{J}_{TE}^{bot} with $J_{TE}^{top} < J_{TE}^{bot}$. The thermoelectric Lorentz forces, \mathbf{F}_{TE}^{top} and \mathbf{F}_{TE}^{bot} , create a net torque $\boldsymbol{\tau}_{net}$ perpendicular to the LSC's angular momentum vector, \mathbf{L}_{LSC} , which drives the LSC to precess around the tank's vertical $\hat{\mathbf{e}}_z$ -axis. (b) Precessional flywheel schematic (not to scale). The LSC is simplified into a flywheel-like cylinder of radius R^* , with angular velocity $\omega_{LSC} \lesssim U_{ff}/R^*$ and angular momentum $\mathbf{L}_{LSC} = \omega_{LSC} M R^{*2} \hat{\mathbf{e}}_x/2$. The LSC is assumed to respond to $\boldsymbol{\tau}_{net}$ in a solid-body manner.

generated across the k -level Cu-Ga interface are then estimated to be

$$\mathbf{F}_{TE}^k = \frac{1}{2} V_{LSC} \mathbf{f}_{TE}^k. \quad (6.11)$$

In order to estimate the torques due to each thermoelectric current loop, we assume that the thermoelectric Lorentz forces act on the LSC via a moment arm $\boldsymbol{\ell}$ of approximate length $H/2$. Thus, $\boldsymbol{\ell}^{top} = H/2 \hat{\mathbf{e}}_z$ and $\boldsymbol{\ell}^{bot} = -H/2 \hat{\mathbf{e}}_z$. The net thermoelectric torque on the LSC then becomes

$$\boldsymbol{\tau}^{net} = \boldsymbol{\tau}^{top} + \boldsymbol{\tau}^{bot} \quad (6.12a)$$

$$= (\boldsymbol{\ell}^{top} \times \mathbf{F}_{TE}^{top}) + (\boldsymbol{\ell}^{bot} \times \mathbf{F}_{TE}^{bot}) \quad (6.12b)$$

$$= (H/2) \hat{\mathbf{e}}_z \times (\mathbf{F}_{TE}^{top} - \mathbf{F}_{TE}^{bot}) \quad (6.12c)$$

$$= (H V_{LSC} / 4) \hat{\mathbf{e}}_z \times (\mathbf{f}_{TE}^{top} - \mathbf{f}_{TE}^{bot}). \quad (6.12d)$$

Substituting eq. (6.9) into eq. (6.12d) yields the net thermoelectric torque on the LSC to be

$$\begin{aligned} \boldsymbol{\tau}^{net} &= \frac{\sigma_0 V_{LSC} X_0 B (T^{bot} \delta T^{bot} - T^{top} \delta T^{top})}{4\Gamma} (\hat{\mathbf{e}}_x \times \hat{\mathbf{e}}_b) \\ &= \frac{\sigma_0 V_{LSC} X_0 B \mathcal{T}}{4\Gamma} (\hat{\mathbf{e}}_x \times \hat{\mathbf{e}}_b), \end{aligned} \quad (6.13)$$

where

$$\mathcal{T} \equiv (T^{bot} \delta T^{bot} - T^{top} \delta T^{top}) \quad (6.14)$$

describes the difference in thermal conditions on the bottom relative to top horizontal Cu-Ga interfaces. Since $T^{bot} > T^{top}$ in all our convection experiments, the data in figure 10(b) implies that $\mathcal{T} > 0$ in the MP regime. Since all the other parameters in eq. (6.13) are positive, the net thermoelectric torque is directed in $-\hat{\mathbf{e}}_y$ for upwards directed magnetic fields ($\hat{\mathbf{e}}_b = +\hat{\mathbf{e}}_z$) and, as shown in figure 13, the net torque is directed

Symbols	Description	Value
σ_0	Cu-Ga effective electric conductivity, eq. (2.5)	3.63×10^6 S/m
B	magnetic field intensity	120 gauss
\mathcal{L}	Horizontal length scale of TE current loops, $\approx \Gamma H$	197.2 mm
X_0	Cu-Ga Seebeck prefactor, eq. (6.6)	-7.89×10^{-9} V/K ²
ρ	Liquid gallium density	6.08×10^3 kg/m ³
R^*	Effective radius of the LSC, eq. (6.1)	0.08 m
U_{ff}	Free-fall velocity, eq. (2.10)	0.03 m/sec
\bar{T}	Mean fluid temperature, eq. (3.5)	42.50 °C
ΔT	Vertical temperature difference across the fluid, eq. (3.3)	7.03 K
T^{bot}	Bottom interface mean temperature	319.23 K
δT^{bot}	Bottom interface mean temperature difference, eq. (5.2)	3.44 K
T^{top}	Top interface mean temperature	312.07 K
δT^{top}	Top interface mean temperature difference, eq. (5.2)	2.24 K
\mathcal{T}	$(T^{bot} \delta T^{bot} - \delta T^{top} \delta T^{top})$	399.11 K ²

TABLE 2. Experimental parameter values from the *Conducting MC⁻* subcase. These values are characteristic of those used in calculating ω_{MP} in figure 14.

in $+\hat{\mathbf{e}}_y$ for downwards directed magnetic fields ($\hat{\mathbf{e}}_b = -\hat{\mathbf{e}}_z$). Eq. (6.13) also shows that the bottom torque will tend to dominate even when $\delta T^{bot} \approx \delta T^{top}$ since $T^{bot} > T^{top}$ in all convectively unstable cases.

6.4. Thermoelectrically-driven LSC Precession

The net thermoelectric torque on the LSC acts in the direction perpendicular to \mathbf{L}_{LSC} . The LSC must then undergo a precessional motion in order to conserve angular momentum. This precession can be quantified via Euler's equation (Landau & Lifshitz 1976), in which the net torque is the time derivative of the angular momentum:

$$\boldsymbol{\tau}^{net} = \frac{d\mathbf{L}_{LSC}}{dt} = I \frac{d\boldsymbol{\omega}}{dt} + \boldsymbol{\omega} \times \mathbf{L}_{LSC}, \quad (6.15)$$

The angular velocity vector $\boldsymbol{\omega}$ is comprised of two components here

$$\boldsymbol{\omega} = \omega_{LSC} \hat{\mathbf{e}}_x + \boldsymbol{\omega}_{MP}, \quad (6.16)$$

where ω_{LSC} is the angular velocity component of the flywheel in $\hat{\mathbf{e}}_x$ and $\boldsymbol{\omega}_{MP}$ is the angular velocity vector of the LSC's magnetoprecession. We assume that the precession frequency and the angular speed of the flywheel are nearly time-invariant, $d\boldsymbol{\omega}/dt \approx 0$. Then eq. (6.15) reduces to

$$\boldsymbol{\tau}^{net} = (\omega_{LSC} \hat{\mathbf{e}}_x + \boldsymbol{\omega}_{MP}) \times L_{LSC} \hat{\mathbf{e}}_x = \boldsymbol{\omega}_{MP} \times L_{LSC} \hat{\mathbf{e}}_x, \quad (6.17)$$

where $\boldsymbol{\omega}_{LSC} \times \mathbf{L}_{LSC} = 0$ since these vectors are parallel. Expression eq. (6.17) requires that $\boldsymbol{\omega}_{MP}$ remain orthogonal to both \mathbf{L}_{LSC} and $\boldsymbol{\tau}^{net}$ such that

$$\boldsymbol{\tau}^{net} (\hat{\mathbf{e}}_x \times \hat{\mathbf{e}}_b) = \boldsymbol{\omega}_{MP} \times L_{LSC} \hat{\mathbf{e}}_x = \omega_{MP} L_{LSC} (\hat{\boldsymbol{\omega}}_{MP} \times \hat{\mathbf{e}}_x). \quad (6.18)$$

Therefore, $\hat{\boldsymbol{\omega}}_{MP} = -\hat{\mathbf{e}}_b$ and the precessional angular velocity vector is

$$\boldsymbol{\omega}_{MP} = \frac{\tau^{net}}{L_{LSC}} (-\hat{\mathbf{e}}_b). \quad (6.19)$$

Substituting eqs. (6.4) and (6.13) into eq. (6.19) yields our analytical estimate for the thermoelectrically-driven angular velocity of LSC precession in the $N_c \lesssim 1$ TEMC experiments:

$$\boldsymbol{\omega}_{MP} = \frac{\sigma_0 X_0 B}{2\rho U_{ff} \Gamma R^*} (T^{bot} \delta T^{bot} - T^{top} \delta T^{top}) (-\hat{\mathbf{e}}_b) \quad (6.20a)$$

$$= \frac{\sigma_0 X_0 B \mathcal{T}}{2\rho U_{ff} \Gamma R^*} (-\hat{\mathbf{e}}_b) \quad (6.20b)$$

$$= \frac{\pi^{1/2}}{\Gamma^{3/2}} \frac{\sigma_0 X_0 B \mathcal{T}}{2\rho U_{ff} H} (-\hat{\mathbf{e}}_b). \quad (6.20c)$$

Expressions (6.19) and eq. (6.20) predict that the LSC's magnetoprecessional angular velocity vector, $\boldsymbol{\omega}_{MP}$, will always be antiparallel to the imposed magnetic field vector in our Cu-Ga TEMC experiments in which $\mathcal{T} > 0$. Further, the magnetoprecession should flip direction such that $\boldsymbol{\omega}_{MP}$ would be parallel to \mathbf{B} in a comparable Cu-Ga TEMC system with $\mathcal{T} < 0$. These predictions agree with the precession directions found in our MP regime experiments, as shown in figure 7(a).

6.5. Experimental Verification

The direction of magnetoprecession is sensitive to the sign of \mathcal{T} . The value and sign of \mathcal{T} are, however, both likely related to the details of the experimental set up. For instance, we have a thermostated bath controlling the top thermal block temperature, whereas a fixed thermal flux is input below the bottom thermal block. Further, the top and bottom thermal blocks have different thicknesses. It is possible that \mathcal{T} could behave differently with much thinner or thicker end-blocks, and for differing thermal boundary conditions. Thus, further modeling efforts are required before \mathcal{T} can be predicted *a priori*.

Figure 14(a) provides a test of our magnetoprecession model using data from the *Conducting MC*⁻ case. The blue line shows the experimentally determined LSC angular velocity via measurements of the azimuthal drift velocity of the LSC plane, $d\xi_j^{mid}/dt$, made with the best fits to eq. (4.1). The magenta line shows the instantaneous angular velocity of LSC precession, $(\omega_{MP})_j$, calculated by feeding instantaneous thermal data from the *Conducting MC*⁻ case into eq. (6.20). The green line is a modified theoretical estimate, in which the U_{MC} velocity prediction (2.27) is used in eq. (6.20) instead of the upper bounding U_{ff} estimate.

The three time series in figure 14(a) show that the predicted magnetoprecessional angular speeds compare well with the LSC azimuthal drift speed, especially when accounting for the simplifications that are underlying eq. (6.20). The time series all have similar gross shapes, but with the peaks in $d\xi_j^{mid}/dt$ slightly delayed in time relative to those in the ω_{MP} curves. The dashed lines in figure 14 show the time-mean angular velocity values. The time mean LSC plane velocity is $d\xi^{mid}/dt = 5.27 \times 10^{-3}$ rad/s. The mean value of the magnetoprecessional flywheel (magenta) is $\omega_{MP} = 2.48 \times 10^{-3}$ rad/s = $0.47 d\xi^{mid}/dt$. The mean value of the modified estimate (green) is $\omega_{MP} U_{ff}/U_{MC} = 3.10 \times 10^{-3}$ rad/s = $0.59 d\xi^{mid}/dt$. Moreover, there is a good agreement between the converted angular speed from the peak frequency $2\pi f_{peak}$ of the FFTs (black dashed lines) and the mean LSC azimuthal drift speed by direct thermal measurement $d\xi^{mid}/dt$ (blue dashed lines). The direct measurement is about 2.5% higher than $2\pi f_{peak}$.

Figure 14(b) shows the correlation between the measured angular velocity $d\xi_j^{mid}/dt$ and \mathcal{T} . The angular velocity values correspond to the blue curve in panel (a). The dashed red line is the best linear fit to the data, and shows that there is a net positive correlation between $d\xi_j^{mid}/dt$ and the asymmetry of the thermal condition in end-blocks, represented

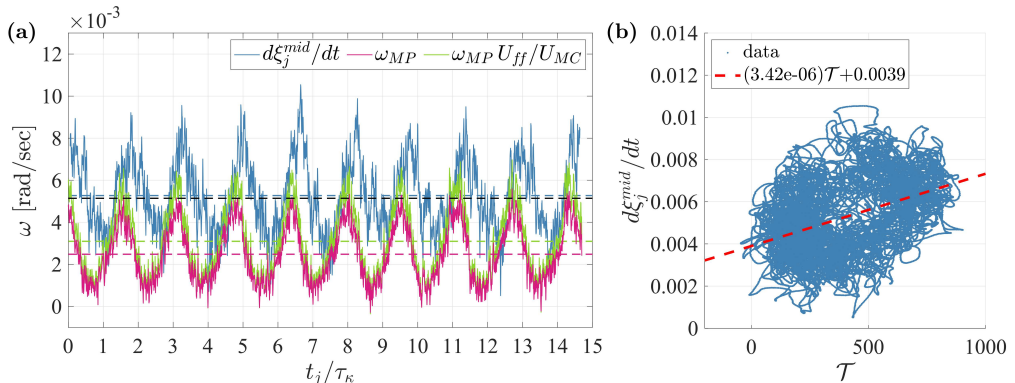


FIGURE 14. (a) Time series of LSC precessional rate for the *Conducting MC⁻* case at $Ra = 1.83 \times 10^6$, $Ch = 2.59 \times 10^3$, and $N_C = 0.31$. The horizontal axis shows time t normalized by the diffusion timescale τ_κ . The vertical axis is the LSC’s instantaneous angular precession speed ω . The blue line shows angular velocity of the LSC plane, $d\xi_j^{mid}/dt$, measured via eq. (4.1) using temperature data on the midplane sidewall. The magenta line marks ω_{MP} model predictions made using eq. (6.20) and instantaneous temperature data. The green line shows the alternative MP prediction made using eq. (6.20) with Zürner *et al.* (2020)’s U_{MC} velocity scaling eq. (2.27). See Appendix Table 4 for *Conducting MC⁻* case details. The horizontal dashed lines are mean values for their corresponding angular speeds. The black horizontal dashed line represents the peak frequency from the FFT converted into the angular speed. (b) Scatter plot of $d\xi_j^{mid}/dt$ versus \mathcal{T} . The red dashed line is a linear fit for this particular case. The best fit slope, $3.42 \times 10^{-6} \text{ K}^2/\text{s}$, is 55.3% of the theoretical prediction from (6.20), where the prefactor $\sigma_0 X_0 B / (4\rho U_{ff} R^*) \approx 6.18 \times 10^{-6} \text{ K}^2/\text{s}$.

by \mathcal{T} . The best fit slope is $(d\xi_j^{mid}/dt)/\mathcal{T} = 3.42 \times 10^{-6} \text{ K}^2/\text{s}$. Theoretical prediction (6.20) gives $\omega_{MP}/\mathcal{T} = \sigma_0 X_0 B / (4\rho U_{ff} R^*) = 6.18 \times 10^{-6} \text{ K}^2/\text{s}$. Thus, the best-fit slope agrees with theory to within approximately a factor of two.

The thermoelectric LSC precession model is tested further in figure 9(a) and figure 15 using the fixed $Ra \approx 2 \times 10^6$ case results. In figure 9(a), the peak of each experiment’s thermal FFT spectrum is marked by an open black circle. The circles in the MP regime are connected by a best fit parabola (black dashed curve). The white stars show the predicted magnetoprecessional frequency, $f_{MP} = \omega_{MP}/2\pi$, calculated using eq. (6.20). The white dotted line is the best parabolic fit to the f_{MP} values. Adequate agreement is found between the spectral peaks and the f_{MP} values. The low frequency tail of the best fits appears to correlate with secondary peaks in the thermal spectra. This suggests that MP modes exist down to $Ch \simeq 10^3$ in the JRV regime, but with weaker spectral signatures that do not dominate those of the jump rope LSC flow.

Figure 15(a) shows a linear plot of FFT spectral peaks (black circles), f_{MP} predictions (magenta stars), and the modified predictions $f_{MP}(U_{ff}/U_{MC})$ (green stars) plotted versus N_C for the fixed $Ra \approx 2 \times 10^6$ MC experiments with $N_C < 1$. The dashed lines show best parabolic fits. The vertical dot-dashed lines are the regime boundaries that separate the JRV, MP and MCMC regimes in figure 9(a). The f_{MP} estimates differs by $\lesssim 37\%$ from the experimental spectral data, while the improved model that makes use of U_{MC} differs from the spectral peak frequencies by $\lesssim 16\%$. Further, the intersections of the best fit parabolas with $f/f_\kappa = 0$, near $N_C \approx 0.1$ and $N_C \approx 1$, agree well with the empirically located regime boundaries.

Figure 15(b) shows $\mathcal{T} = (T^{bot}\delta T^{bot} - T^{top}\delta T^{top})$ versus N_C for the experimental cases shown in panel (a). Although it resembles the curves in panel (a), the shape of the \mathcal{T} curve is steeper on its $N_C < 0.4$ branch and its peak is shifted to slightly lower N_C .

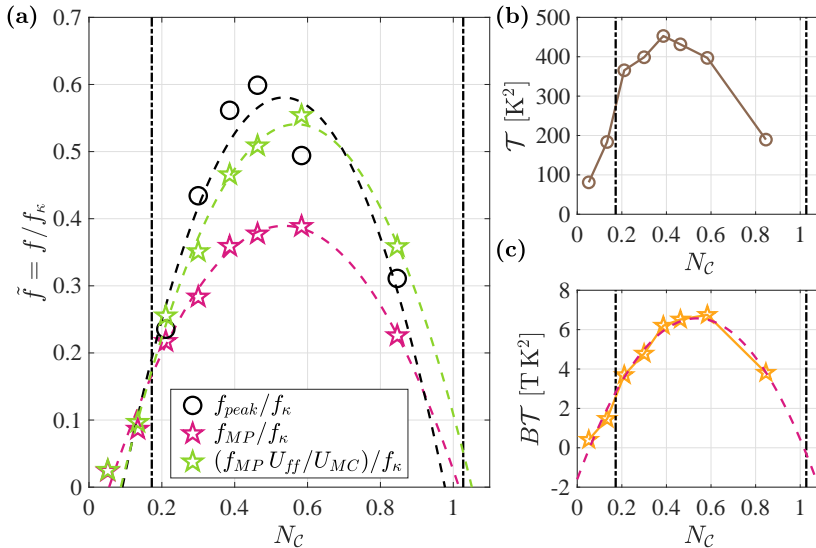


FIGURE 15. (a) Normalized precessional frequency, $\tilde{f} = f/f_\kappa$, versus convective interaction parameter, N_C , where the thermal diffusion frequency is $f_\kappa \equiv 1/\tau_\kappa \approx 1.34 \times 10^{-3}$ Hz. Black circles denote the peak frequencies of FFT spectra for the fixed $Ra \approx 2 \times 10^6$ experimental survey. Magenta stars are frequencies predicted by the TEMPC precession model, $f_{MP}/f_\kappa = \omega_{MP}/(2\pi f_\kappa)$. Green stars correspond to $\omega_{MP}U_{ff}/(2\pi U_{MC}f_\kappa)$, the frequency of the precession model using the U_{MC} scaling velocity. Dashed curves represent the second-order best fit curves. (b) τ versus N_C . (c) The product BT versus N_C . The magenta dashed curve is the second degree best fit curve from panel (a) normalized by the factor $\sigma_0 X_0 / (8\pi f_\kappa \rho U_{ff} R^*) \approx 0.0612 [\text{T}^{-1} \text{K}^{-2} \text{s}^{-1}]$.

Figure 15(c) shows the product BT plotted in orange as a function of N_C . The magenta dashed curve in Figure 15(c) is the best fit parabolic curve from panel (a) normalized by $8\rho U_{ff} R^* / (\sigma_0 X_0)$, which, according to eq. (6.20), separates these values. By comparing figures 15(b) and 15(c), we argue that the quasi-parabolic structure of the MP frequency data in the MP regime is controlled by trade-offs between the B and τ trends.

7. Discussion

We have conducted a series of magnetoconvection (MC) laboratory measurements in turbulent liquid gallium convection with a vertical magnetic field and thermoelectric (TE) currents in cases with electrically-conducting boundaries. Three regimes of TEMC flow are found: i) the LSC sustains its flow structure in the $0 < N_C \lesssim 0.1$ jump rope vortex (JRV) regime; ii) long-period magnetoprecession (MP) of the LSC dominates the $0.1 \lesssim N_C \lesssim 1$ MP regime; and iii) the LSC is replaced by a multi-cellular magnetoconvective flow pattern in the $N_C \gtrsim 1$ MCMC regime.

Figure 16(a) shows the convective and thermoelectric interaction parameters, N_C and N_{TE} respectively, as a functions of Ch . The vertical dashed lines separate the parameter space into the three characteristic regimes in figure 9, with JRV on the left hand side, MP in the middle and MCMC on the right hand side. Both N_C and N_{TE} are approximately of the same order in the MP regime. The blue open triangles correspond to the experimentally derived thermoelectric interaction parameters at the bottom boundary for the fixed- Ra survey, $N_{TE}^{bot} = \sigma B |\tilde{S}| \delta T^{bot} / (\rho U_{ff}^2)$. The bottom boundary temperature data, δT^{bot} , are used here because it has the larger N_{TE} than the top layer, and dominates the dynamics of the magnetoprecession.

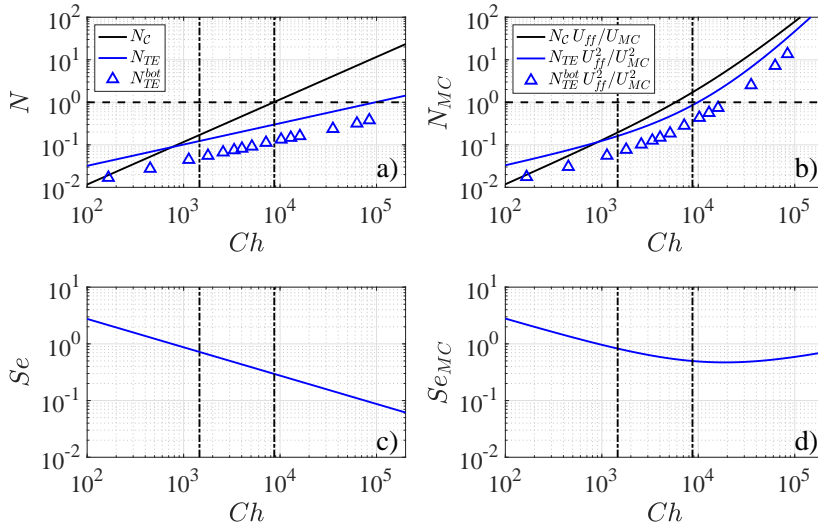


FIGURE 16. a) Convective and thermoelectric interaction parameters, N_C and N_{TE} , plotted versus Chandrasekhar number Ch over the parameter space of the fixed- Ra survey. The black line shows $N_C = \sigma B^2 H / (\rho U_{ff})$, and the blue line shows $N_{TE} = \sigma B |\tilde{S}| \Delta T / (\rho U_{ff}^2)$, following the definitions in eq. (2.22) and eq. (2.23). The net Seebeck coefficient $\tilde{S} = X_0 \bar{T}$ is defined using the mean temperature of the system. The blue triangles denote $N_{TE}^{bot} = \sigma B |\tilde{S}| \delta T^{bot} / (\rho U_{ff}^2)$ calculated for the experimental data of the fixed- Ra cases. The two vertical black dot-dashed lines separate the parameter space into the JRV, MP and MCMC regimes from left to right in each panel. Panel (b) is comparable to (a), but employs the characteristic MC flow speed U_{MC} in place of U_{ff} . Panels (c) and (d) show the corresponding Seebeck numbers, $Se = N_{TE}/N_C$ and $Se_{MC} = (N_{TE}/N_C) (U_{ff}/U_{MC})$, respectively.

Figure 16(b) uses U_{MC} as the characteristic flow speed instead of U_{ff} . Similar to (a), both N_C and N_{TE} are of the same order and roughly aligned with each other in the MP regime, which means the quasistatic Lorentz forces from the fluid motions are comparable to the thermoelectric Lorentz forces. Panels (c) and (d) show Se and Se_{MC} , which are the ratios of the blue and black lines in panels (a) and (b), respectively. Since the convective and TE interaction parameters are order unity in the MP regime in figure 16, this shows that both the Lorentz forces are approximately comparable to the buoyant inertia. Thus, a triple balance is possible between the motionally-induced Lorentz forces, the thermoelectric Lorentz forces and the buoyancy forces in the MP regime.

Our thermoelectrically-driven precessional flywheel model provides an adequate characterization of the MP mode that is observed in turbulent MC experiments with electrically conducting boundaries. The model predicts the zeroth-order precessional frequencies of the MP mode. Further, it explains the changing direction of precession when the imposed magnetic field direction is reversed (figure 7).

There are, however, a number of limitations to our flywheel model. First, we have allowed Ga to corrode the Cu end-blocks in order to ensure good material contact across the interfaces. The reaction between Cu and Ga forms a gallium alloy layer on the copper boundary. This ongoing reaction should decrease the interfacial electrical conductivity over time, resulting in a smaller net torque on the LSC and a slower rate of magnetoprecession. This may explain a subtle feature in figure 9: the peak frequency from the MC^- case is higher than the comparable fixed- Ra survey case that was carried out months later but with similar control parameters. Thus, Ga-Cu chemistry at the interface appears to matter in the TE dynamics, yet we are currently unable to

control or to parameterize these interfacial reaction processes. Second, our model requires measurements of the horizontal temperature gradients in the conducting end-blocks. A fully self-consistent model would use the input parameters to predict these gradients *a priori*, independent of the experimental data.

A long-period precessional drift of the LSC has also been observed in water-based laboratory experiments influenced by the Earth's rotation (Brown & Ahlers 2006). In their experiments, the LSC rotates azimuthally with a period of days. This period is over two orders of magnitude greater than our MP period. Since MP modes are found only to develop in the presence of imposed vertical magnetic fields and electrically-conducting boundaries, it is not possible to explain the MP mode solely due to Coriolis effects from Earth's rotation.

Alternatively, the rotation of the Earth could couple with the magnetic field to induce magneto-Coriolis (MC) waves in the convecting gallium (e.g., Finlay 2008; Hori *et al.* 2015; Schmitt *et al.* 2013). In the limit of strong rotation, MC waves have a slow branch that might appear to be relevant to our experimental MP data. However, our current TEMC experiments are stationary in the lab frame and, thus, are only spun by Earth's rotation, similar to Brown & Ahlers (2006) and unlike King & Aurnou (2015). They therefore exist in the weakly rotating MC wave limit. As shown in Appendix B, the weakly rotating MC wave dispersion relation can be reduced to

$$\omega_{MC} = \pm \left(\frac{\mathbf{B} \cdot \mathbf{k}_0}{\sqrt{\rho\mu}} (1 \pm \epsilon) \right) \approx \omega_A, \quad \text{where} \quad \epsilon = \frac{\sqrt{\rho\mu}}{k_0} \frac{\boldsymbol{\Omega} \cdot \mathbf{k}_0}{\mathbf{B}_0 \cdot \mathbf{k}_0} \ll 1, \quad (7.1)$$

\mathbf{k}_0 is the wavevector, $\boldsymbol{\Omega}$ is the angular velocity vector, \mathbf{B} is the applied magnetic flux density, μ is the magnetic permeability and $\omega_A = \pm(\mathbf{B} \cdot \mathbf{k}_0)/\sqrt{\rho\mu}$ is the Alfvén wave dispersion relation. With $\epsilon \simeq 4 \times 10^{-6} \text{ s}^{-1}$ in our experiments, the MC wave period is well approximated by an Alfvén wave timescale $\tau_A = H/(B/\sqrt{\rho\mu})$ that is typically less than 1 s in our system. For instance, $\tau_A \simeq 0.74 \text{ s}$ for the *Conducting MC*⁻ case, a value three orders of magnitude shorter than the observed MP periods. Thus, we conclude that the MP mode is best explained via TEMC dynamics.

Turbulent magnetoconvection is relevant for understanding many geophysical and astrophysical phenomena (e.g., Proctor & Weiss 1982; King & Aurnou 2015; Vogt *et al.* 2021). If $\tilde{S} \approx 0$ under planetary interior conditions (e.g., Chen *et al.* 2019), then thermoelectric currents can exist in the vicinity of the core-mantle boundary (CMB) and inner core boundary of Earth's liquid metal outer core and those of other planets. Assuming Se is not trivially small across these planetary interfaces, then TEMC-like dynamics could influence planetary core processes and could prove important for our understanding of planetary magnetic field observations (e.g., Merrill & McElhinny 1977; Stevenson 1987; Schneider & Kent 1988; Giampieri & Balogh 2002; Meduri *et al.* 2020). Previous models of planetary core thermoelectricity have focused predominantly on magnetic fields produced as a byproduct of CMB thermoelectric current loops (Stevenson 1987; Giampieri & Balogh 2002). In contrast, our experimental results suggest that TE processes can generate 'slow modes,' which could change a body's observed magnetic field by altering the local CMB magnetohydrodynamics. Further, thermoelectric effects provide a \mathbf{B} -dependent symmetry-breaker that does not exist in current models of planetary core magnetohydrodynamics.

Two dominant structures are known to exist at the base of Earth's mantle: thermochemical piles (Trampert *et al.* 2004; Mosca *et al.* 2012; Garnero *et al.* 2016; Deschamps *et al.* 2018) and ultra low velocity zones (ULVZs) (Garnero *et al.* 1998), both shown schematically in figure 17. Seismic tomographic inversions reveal that the continental-sized thermochemical piles have characteristic length scales of approximately

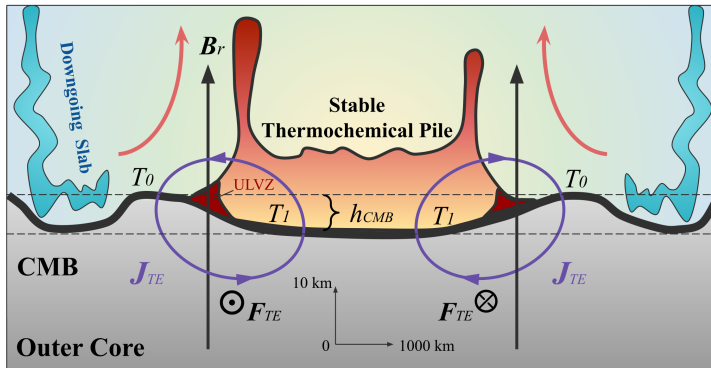


FIGURE 17. Schematic adapted from Garnero *et al.* (2016) and Deschamps *et al.* (2018) showing thermoelectric currents \mathbf{J}_{TE} and forces \mathbf{F}_{TE} in the vicinity of the core-mantle boundary (CMB). The vertical scale is considerably exaggerated. The black arrows are radial magnetic field, $B_r \sim 19$ gauss. The temperature contrast between the thermochemical pile or the ULVZs and the surrounding mantle is denoted by $T_1 - T_0 = \Delta T_p \sim 10^2$ K. The dynamic depression of the CMB, $h_{CMB} \sim 5$ km, can generate smaller adiabatic temperature differences of order 5 K.

5000 km along the CMB (Cottaar & Lekic 2016; Garnero *et al.* 2016). The ULVZs are patches a few tens of kilometers thick just above the CMB where the seismic shear wave speed is about 30% lower than the surrounding material (Garnero *et al.* 1998). The lateral length scale of ULVZs ranges from 10 km (Garnero *et al.* 2016) to over 1000 km based on recent studies of so-called mega-ULVZs (Thorne *et al.* 2020, 2021). Lateral thermal gradients can exist along the CMB between the piles or ULVZs and surrounding regions. By estimating the excess temperature of mantle plumes (Bunge 2005) or by taking the temperature difference between the ULVZ melt (e.g., Liu *et al.* 2016; Li *et al.* 2017) and cold slabs (Tan *et al.* 2002) near the CMB, we argue that the lateral temperature difference on the CMB to be $\lesssim 3 \times 10^2$ K. Therefore, the lateral thermal gradient across the edge of ULVZs is possibly on the order of magnitude of 1 K/km.

On the fluid core side of the CMB, Mound *et al.* (2019) have argued that the outer core fluid situated just below the thermochemical piles will tend to form regionally stably-stratified lenses. If such lenses exist, thermal gradients will also exist in the outer core across the boundaries between the stable lenses, where the heat flux is subadiabatic, and the surrounding convective regions. ULVZs may have high electrical conductivity due to iron enrichment and silicate melt (Holmström *et al.* 2018), such that the electrical conductivity is $\sigma \simeq 3.6 \times 10^4$ S/m at CMB-like condition (136 GPa and 4000 K). Therefore, these structures may prove well-suited to host TE current loops.

In Earth's core, we take the radial magnetic field strength B_r to be of order 1 mT on the CMB and estimate the flow speed to be $U_C \sim 0.1$ mm/s, based on inversions of geomagnetic field data (Holme 2015; Finlay *et al.* 2016). Note that the outer core flow velocity might be lower if there are convectively stable layers (Buffett & Seagle 2010) or stable fluid lenses (Mound *et al.* 2019) situated below the CMB. Seebeck numbers across Earth's core-mantle boundary may then be estimated as

$$Se = \frac{|\tilde{S}|\Delta T_p}{U_C B_r L_p} \text{ for the thermochemical piles,} \quad (7.2a)$$

$$Se = \frac{|\tilde{S}|\Delta T_p}{U_C B_r L_{ulvz}} \text{ for the ULVZs,} \quad (7.2b)$$

Parameters	Description	Estimates
ΔT_p	Lateral temperature difference between the thermochemical pile and its surrounding mantle in the CMB	~ 300 K
U_C	Outer core flow speed near CMB	~ 0.1 mm/s
B_r	Radial geomagnetic field at the CMB	~ 1 mT
L_p	Characteristic length of a thermochemical pile	~ 5000 km
L_{ulvz}	Characteristic length of the ULVZs	~ 500 km

TABLE 3. Parameters used to estimate Seebeck numbers (7.2) across Earth’s core-mantle boundary (CMB).

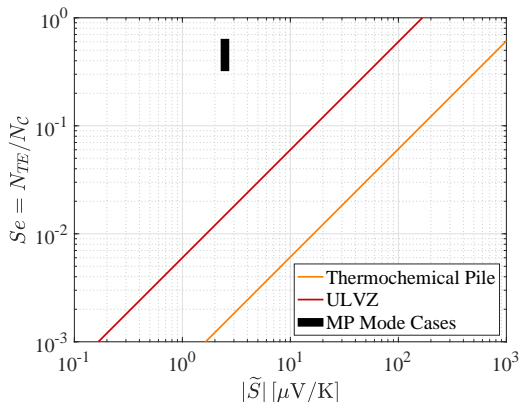


FIGURE 18. The Seebeck number Se as a function of the net Seebeck coefficient \tilde{S} . The red (orange) line represents estimated values for ULVZs (thermochemical piles) via eqs. (7.2). The thick black line marks the range of cases that have magnetoprecessional modes in this study. Here, \tilde{S} is defined with the mean temperature of the fluid, \bar{T} , so that $\tilde{S} = X_0 \bar{T}$. Our experiments show that TEMC dynamics can emerge at Se below unity.

where $\Delta T_p \sim 300$ K is taken to be the lateral temperature difference between the thermochemical piles and the surrounding mantle.

Figure 18 shows estimated CMB Seebeck numbers as a function of the net Seebeck coefficient \tilde{S} . The orange line represents the thermochemical pile with a characteristic length $L_p \sim 5 \times 10^3$ km. The red line represents the ULVZ with a characteristic length $L_{ulvz} \sim 500$ km. The cases from this study that have MP modes are denoted by a thick black line. The Seebeck number is defined as $Se = |\tilde{S}| \Delta T / (U_{ff} B H)$, with \tilde{S} defined with the mean temperature of the fluid, \bar{T} , so that $\tilde{S} = X_0 \bar{T}$. Our experimental results show TEMC dynamics emerge at Se below 1. This plot suggests then that net Seebeck coefficients at the CMB must exceed values of order $10 \mu\text{V/K}$ in order for TEMC dynamics to affect Earth’s local CMB dynamics and possibly alter the observed magnetic field.

We do not know at present if \tilde{S} can actually attain the values necessary to drive significant thermoelectric currents across planetary core interfaces. It should be noted that many thermoelectric materials, especially semiconductors, are known to have large Seebeck coefficients that can exceed $100 \mu\text{V/K}$. Silicon, for instance, has a Seebeck coefficient of $\sim 800 \mu\text{V/K}$ at 500 K (Fulkerson *et al.* 1968). Moreover, recent studies in thermoelectric materials show that Seebeck coefficients can increase with increasing

pressures and temperatures (Chen *et al.* 2019; Morozova *et al.* 2019; Yoshino *et al.* 2020). How the TE coefficients of deep Earth materials extrapolate to core-mantle boundary conditions has, however, yet to be determined.

Acknowledgements

This manuscript was greatly improved thanks to feedback given by three anonymous referees. We further thank Ashna Aggarwal, Xiyuan Bao, Paul Davis, Carolina Lithgow-Bertelloni, Lars Stixrude, and Tobias Vogt for fruitful discussions, and Jewel Abbate and Taylor Lonner for help with the experiments. The authors also gratefully acknowledge the support of the NSF Geophysics Program (EAR awards 1620649 and 1853196).

Declaration of Interests

The authors report no conflict of interest.

Appendix A. Nondimensional Equations

The governing equations (2.15) can be nondimensionalized using H as length scale and U_{ff} as the velocity scale, such that the free-fall time $\tau_{ff} = H/U_{ff}$ is the time scale. Moreover, the external magnetic flux density B is the magnetic field scale, the bulk current density is scaled by $\sigma U_{ff} B$, the electric potential scale is $U_{ff} B H$, and ΔT is the temperature scale.

The dimensionless governing equations of Oberbeck-Boussinesq thermoelectric magnetoconvection (TEMC) are

$$\nabla \cdot \mathbf{J} = 0, \quad (\text{A } 1a)$$

$$\mathbf{J} = -\nabla\Phi + \mathbf{u} \times \hat{\mathbf{e}}_b - Se\nabla T, \quad (\text{A } 1b)$$

$$\nabla \cdot \mathbf{u} = 0, \quad (\text{A } 1c)$$

$$\frac{\partial \mathbf{u}}{\partial t} + \mathbf{u} \cdot \nabla \mathbf{u} = -\nabla p + \sqrt{\frac{Ch^2 Pr}{Ra}} (\mathbf{J} \times \hat{\mathbf{e}}_b) + \sqrt{\frac{Pr}{Ra}} \nabla^2 \mathbf{u} + T \hat{\mathbf{e}}_z, \quad (\text{A } 1d)$$

$$\frac{\partial T}{\partial t} + \mathbf{u} \cdot \nabla T = \sqrt{\frac{1}{Ra Pr}} \nabla^2 T, \quad (\text{A } 1e)$$

where here \mathbf{u} is the dimensionless velocity of the fluid, p is the dimensionless non-hydrostatic pressure, \mathbf{J} is the dimensionless electric current density, $\mathbf{B} = \hat{\mathbf{e}}_b$ is the dimensionless flux density of the external magnetic field, and T is the nondimensional temperature. The nondimensionalized vertical magnetic field is constant and uniform, $\hat{\mathbf{e}}_b = \pm \hat{\mathbf{e}}_z$.

The $(Ra/Pr)^{-1/2}$ grouping in (A 1d) is the reciprocal of the Reynolds number Re . The $(RaPr)^{-1/2}$ group in (A 1e) is the reciprocal of the Péclet number. Further, using (A 1b), the Lorentz term in (A 1d) expands to:

$$\begin{aligned} \sqrt{\frac{Ch^2 Pr}{Ra}} (\mathbf{J} \times \hat{\mathbf{e}}_b) &= (N_C [-\nabla\Phi + \mathbf{u} \times \hat{\mathbf{e}}_b] - N_{TE} \nabla T) \times \hat{\mathbf{e}}_b \\ &= N_C [(\hat{\mathbf{e}}_b \times \nabla\Phi) - \mathbf{u}_\perp] + N_{TE} (\hat{\mathbf{e}}_b \times \nabla T), \end{aligned} \quad (\text{A } 2)$$

where \mathbf{u}_\perp is the velocity perpendicular to the vertical direction \mathbf{e}_z . The first term on the right-hand side is due to irrotational electric fields in the fluid, which are likely small in our experiments. The second term is the quasi-static Lorentz drag, and the third term is due to thermoelectric currents in the fluid. The nondimensional groups in (A 2) are the convective interaction parameter, $N_C = Ch\sqrt{Pr/Ra}$, and the thermoelectric interaction parameter, $N_{TE} = Se N_C$.

Appendix B. Weakly rotating Magneto-Coriolis Waves

The dispersion relation for the Magnetic-Coriolis wave is (Finlay 2008)

$$\omega_{MC} = \pm \frac{\boldsymbol{\Omega} \cdot \mathbf{k}_0}{k_0} \pm \left(\frac{(\boldsymbol{\Omega} \cdot \mathbf{k}_0)^2}{k_0^2} + \frac{(\mathbf{B} \cdot \mathbf{k}_0)^2}{\rho\mu} \right)^{1/2}, \quad (\text{B } 1)$$

where \mathbf{k}_0 is the wavenumber, $\boldsymbol{\Omega}$ is the angular rotation vector, and \mathbf{B} is the magnetic flux density. In the weakly rotating limit, the Alfvén wave frequency, ω_A , is much larger

than the inertial wave frequency: $|\mathbf{B} \cdot \mathbf{k}/\sqrt{\rho\mu}| \gg |2\boldsymbol{\Omega} \cdot \mathbf{k}_0/k_0|$. The dispersion relation can then be rewritten as

$$\omega_{MC} = \pm \frac{\boldsymbol{\Omega} \cdot \mathbf{k}_0}{k_0} \pm \frac{\mathbf{B} \cdot \mathbf{k}_0}{\sqrt{\rho\mu}} \left(1 + \frac{(\boldsymbol{\Omega} \cdot \mathbf{k}_0)^2 \rho\mu}{(\mathbf{B} \cdot \mathbf{k}_0)^2 k_0^2} \right)^{1/2}. \quad (\text{B } 2)$$

The last term of eq. (B 2) is small, allowing us to carry out a Taylor expansion,

$$\omega_{MC} = \pm \frac{\boldsymbol{\Omega} \cdot \mathbf{k}_0}{k_0} \pm \frac{\mathbf{B} \cdot \mathbf{k}_0}{\sqrt{\rho\mu}} \left(1 + \frac{(\boldsymbol{\Omega} \cdot \mathbf{k}_0)^2 \rho\mu}{2(\mathbf{B} \cdot \mathbf{k}_0)^2 k_0^2} \right). \quad (\text{B } 3)$$

A small quantity ϵ can be defined as:

$$\epsilon = \frac{\sqrt{\rho\mu}}{k_0} \frac{\boldsymbol{\Omega} \cdot \mathbf{k}_0}{\mathbf{B} \cdot \mathbf{k}_0} \ll 1. \quad (\text{B } 4)$$

Eq. (B 3) can then be recast with ϵ ,

$$\omega_{MC} = \pm \frac{\mathbf{B} \cdot \mathbf{k}_0}{\sqrt{\rho\mu}} \left(\epsilon \pm \left(1 + \frac{1}{2}\epsilon^2 \right) \right). \quad (\text{B } 5)$$

Two branches of solution emerge: the fast branch, ω_{MC}^f , is acquired when the first two signs in eq. (B 5) are the same. In contrast, the slow branch, ω_{MC}^s , is acquired when the first two signs in eq. (B 5) are the opposite. Therefore, the slow branch solution will have a smaller absolute values than the fast branch. The solution becomes

$$\left. \begin{aligned} \omega_{MC}^f &= \pm \frac{\mathbf{B} \cdot \mathbf{k}_0}{\sqrt{\rho\mu}} \left(\frac{1}{2}(1 + \epsilon)^2 + \frac{1}{2} \right); \\ \omega_{MC}^s &= \pm \frac{\mathbf{B} \cdot \mathbf{k}_0}{\sqrt{\rho\mu}} \left(\frac{1}{2}(1 - \epsilon)^2 + \frac{1}{2} \right). \end{aligned} \right\} \quad (\text{B } 6)$$

We can further simplify this dispersion relation by applying another Taylor expansion, $(1 \pm \epsilon)^2 \approx 1 \pm 2\epsilon$, such that:

$$\left. \begin{aligned} \omega_{MC}^f &= \pm \frac{\mathbf{B} \cdot \mathbf{k}_0}{\sqrt{\rho\mu}} (1 + \epsilon) \approx \omega_A; \\ \omega_{MC}^s &= \pm \frac{\mathbf{B} \cdot \mathbf{k}_0}{\sqrt{\rho\mu}} (1 - \epsilon) \approx \omega_A. \end{aligned} \right\} \quad (\text{B } 7)$$

Thus, both fast and slow Magnetic-Coriolis waves behave as Alfvén waves in the weakly rotating limit.

Appendix C. Comparison of $\Gamma = 1$ and $\Gamma = 2$ Geometries

To broaden our understanding of TEMC dynamics, here we compare and contrast a set of $\Gamma = 1$ experiments with comparable $\Gamma = 2$ cases. Using the same setup as described in the main text, the $H \simeq 10$ cm sidewall ($\Gamma = 2$) is exchanged with an $H \simeq 20$ cm sidewall to create an experimental device with a $\Gamma = 1$ tank geometry.

Figure 19 shows Hovmöller plots of the sidewall temperature field in four separate experimental cases, one RBC case and one *Conducting MC*⁻ case in each geometry. Figure 19(b) shows that the thermal field precesses in the $\Gamma = 1$ *Conducting MC*⁻ case, similarly to the MP behavior found in $\Gamma = 2$ experiments. The $\Gamma = 1$ magnetoprecession rate is $d\xi_j^{mid}/dt = 8.40 \times 10^{-3}$ rad/s. Our model predicts the angular frequency of

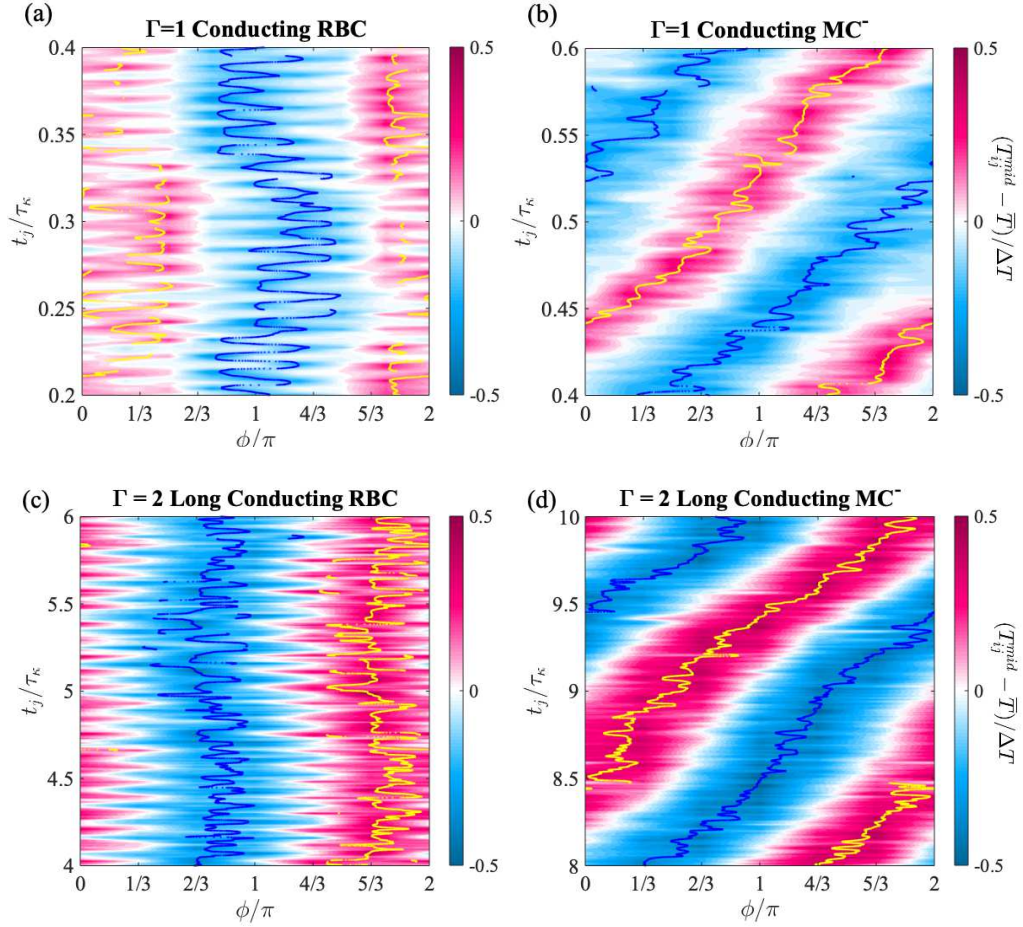


FIGURE 19. Hovmöller diagrams of the sidewall midplane temperature fluctuation. (a) *Conducting RBC* case in the $\Gamma = 1$ tank at $Ra = 2 \times 10^7$, showing the zig-zag pattern characteristic for sloshing. (b) Corresponding *Conducting MC⁻* case at ($Ra = 2.8 \times 10^7$, $Ch = 4.1 \times 10^4$; $N_C = 1.27$, $N_{TE} = 0.16$) showing a drifting magnetoprecession mode. (c) *Long Conducting RBC* case in $\Gamma = 2$ tank at $Ra = 1.79 \times 10^6$ (same as in the main manuscript), showing the accordion pattern characteristic for a jump rope vortex (JRV). (d) Corresponding *Long Conducting MC⁻* at ($Ra = 1.82 \times 10^6$, $Ch = 2.6 \times 10^3$; $N_C = 0.31$, $N_{TE} = 0.16$), showing a drifting magnetoprecession mode similar to (b). The yellow (blue) lines indicate the position of the maximum (minimum) temperature obtained with the TEE method. The time windows are selected to show approximately one full precession, corresponding, respectively, to $0.2\tau_\kappa$ for $\Gamma = 1$ and to $2\tau_\kappa$ for $\Gamma = 2$.

magnetoprecession to be $\omega_{MP}(U_{MC}/U_{ff}) = 6.22 \times 10^{-3}$ rad/s, which is in good zeroth order agreement with the data.

The biggest difference then between the $\Gamma = 1$ and 2 cases is found to be the internal oscillation mode of the LSC. We have previously demonstrated in convection cells with $\Gamma = 2$ that the dominant LSC mode is a jump rope vortex (JRV), whereas in $\Gamma = 1$ the dominant mode is the coupled sloshing-torsional mode (Vogt *et al.* 2018a), see especially the Supplementary Material. Brown & Ahlers (2009) and Zhou *et al.* (2009) have shown that the sloshing and torsional mode are contained in the very same advected oscillation.

Therefore, both modes have the same frequency but a phase difference of π , and the torsional mode cannot exist without a sloshing mode.

We have verified this behaviour in our current set-up. The Conducting RBC case in $\Gamma = 1$ (figure 19(a)) shows a zigzag pattern, which is characteristic for sloshing. The Conducting RBC case in $\Gamma = 2$ (figure 19(c)) shows an accordion pattern, which is characteristic for the jump rope vortex (JRV). In Vogt *et al.* (2018a), we have demonstrated that this is the most straightforward method to identify either mode. In the magnetoconvection cases (figure 19(b,d)), both the sloshing and the JRV modes are suppressed by the magnetoprecession mode, which manifests itself through a strong azimuthal drift of the temperature pattern. But there are faint indications in the MC cases that a much weakened sloshing mode still exists in $\Gamma = 1$ cases, and similarly a much weakened JRV mode still exists in $\Gamma = 2$ cases. The latter is further supported by the spectral data shown in figure 9(a).

We have analysed our data more quantitatively by applying the TEE method of Zhou *et al.* (2009) to the sidewall midplane, top, and bottom temperature measurements, as also indicated by the yellow and blue lines in figure 19. These TEE measurements confirm the existence of the torsional mode in our $\Gamma = 1$ tank by measuring the difference in the azimuthal angles of the best-fit extrema between top and bottom (not shown). We did not find clear evidence of torsional oscillations in the $\Gamma = 2$ cases, neither in the *Insulating* and *Conducting RBC* cases nor in the *Insulating MC*[±], in agreement with the previous $\Gamma = 2$ results of Vogt *et al.* (2018a).

Appendix D. Data Tables

<i>Cases</i>	<i>Bi</i>	<i>B</i> (Gs)	\bar{T} (°C)	ΔT (K)	<i>P</i> (W)	<i>Ra</i> ($\times 10^{-6}$)	<i>Ch</i> ($\times 10^{-3}$)	<i>N_C</i>	<i>N_{TE}</i>	<i>Rm</i> ($\times 10^2$)	<i>Nu</i>	<i>f/f_κ</i>	<i>t/τ_κ</i>
<i>Insulating MC⁻</i>	0.24	-120	42.86	6.79	393.26	1.61	2.42	0.31	0	1.31	5.79±0.09	-	13.6
<i>Insulating RBC</i>	0.24	0	42.86	6.83	393.26	1.61	0	0	0	1.31	5.76±0.09	-	15.2
<i>Insulating MC⁺</i>	0.24	120	42.85	6.79	393.24	1.61	2.41	0.31	0	1.31	5.79±0.09	-	14.0
<i>Conducting MC⁺</i>	0.14	120	42.47	7.02	396.07	1.83	2.57	0.31	0.16	1.40	5.83±0.07	0.71	15.3
<i>Conducting RBC</i>	0.15	0	42.45	6.91	396.12	1.80	0	0	0	1.39	5.93±0.09	11.02	17.0
<i>Conducting MC⁻</i>	0.14	-121	42.50	7.03	396.04	1.83	2.59	0.31	0.16	1.40	5.82±0.08	0.61	15.8
<i>Long Conducting MC⁺</i>	0.14	120	42.45	7.01	396.16	1.82	2.58	0.31	0.16	1.40	5.84±0.07	0.67	37.4
<i>Long Conducting RBC</i>	0.15	0	42.41	6.88	396.19	1.79	0	0	0	1.39	5.96±0.09	11.07	36.1
<i>Long Conducting MC⁻</i>	0.14	-120	42.44	6.99	396.16	1.82	2.59	0.31	0.16	1.40	5.86±0.08	0.64	40.1
<i>Γ = 1 Conducting RBC</i>	0.16	0	44.47	9.89	627.83	20.57	0	0	0	4.68	13.10±0.13	109.52	2.4
<i>Γ = 1 Conducting MC⁻</i>	0.16	-234	52.79	13.00	835.49	28.06	40.92	1.23	0.16	5.36	13.24±0.10	4.59	3.7

TABLE 4. Data and parameters of nine long-period MC^+ , RBC , and MC^- experiments in a $\Gamma = 2$ cell with electrically conducting copper end-blocks and electrically insulating Teflon end-blocks, respectively; and two $\Gamma = 1$ *Conducting RBC* and MC^- cases. In all the cases above, $Pm = 1.69 \times 10^{-6}$, and $Pr = 0.0267$. The precessional frequencies for both long/short groups differ by $\lesssim 5\%$. The Biot number Bi shown in this table is the average Biot number of the top and bottom thermal blocks. B denotes the magnetic flux density; \bar{T} is the time-averaged temperature of the top and bottom plates; ΔT is the temperature difference across the tank height; P is the net power input with heat loss correction; Ra is the Rayleigh number; Ch is the Chandrasekhar number; N_C is the convective interaction parameter; N_{TE} is the thermoelectric interaction parameter, defined in eq. (2.23); Rm is the free-fall estimate of magnetic Reynolds number; Nu is the Nusselt number; f/f_κ is the peak frequency of the averaged spectrum over six sidewall thermistors, normalized by the thermal diffusion frequency; and t/τ_κ denotes the time duration of each case in thermal diffusion timescale $\tau_\kappa = H^2/\kappa$, after the time series data reached statistical equilibrium. Each case is equilibrated for at least 30 min ($> 2\tau_\kappa$). The long conducting cases lasted for about ≈ 113 thermal diffusion time, whereas the short conducting cases lasted for ≈ 48 thermal diffusion time. The insulating cases lasted for ≈ 43 thermal diffusion time.

$B(\text{Gs})$	$\bar{T}(\text{°C})$	$\Delta T(\text{K})$	$P(\text{W})$	$Ra(\times 10^{-6})$	Ra/Ra_A^∞	Ra/Ra_W^∞	Ch	N_C	N_{TE}	$Re(\times 10^{-3})$	$Rm(\times 10^2)$	Nu	f/f_κ	f_{jrv}/f_κ	t/τ_κ
0	40.99	8.19	444.78	2.12	-	-	0.00	0.00	0.00	8.85	1.51	5.61±0.17	11.34	11.34	53.43
-12	40.59	7.91	424.72	2.04	7945.81	710.06	26.00	0.003	0.02	8.72	1.49	5.55±0.17	11.19	11.19	45.41
-30	42.20	7.77	416.10	2.02	1238.28	242.21	1.66×10^2	0.02	0.04	8.67	1.47	5.53±0.16	11.11	11.11	66.80
-50	42.22	7.77	416.09	2.02	455.96	133.53	4.50×10^2	0.05	0.07	8.67	1.47	5.53±0.15	10.98	10.98	53.44
-80	40.71	7.44	393.93	1.92	172.20	72.23	1.13×10^3	0.13	0.10	8.43	1.44	5.47±0.10	10.66	10.66	28.05
-101	40.67	7.52	393.95	1.94	110.05	54.92	1.79×10^3	0.21	0.13	8.49	1.45	5.41±0.07	0.24	9.56	46.75
-120	40.73	7.64	394.08	1.97	77.98	44.50	2.57×10^3	0.30	0.16	8.55	1.46	5.33±0.08	0.43	8.82	66.78
-137	40.69	7.81	394.33	2.02	61.23	38.50	3.34×10^3	0.39	0.18	8.66	1.48	5.22±0.07	0.56	-	53.43
-151	40.85	7.88	393.83	2.04	51.31	34.52	4.02×10^3	0.46	0.20	8.73	1.49	5.17±0.07	0.60	-	60.11
-170	40.91	7.97	393.80	2.06	40.94	30.01	5.10×10^3	0.58	0.22	8.73	1.49	5.10±0.13	0.49	-	66.79
-201	40.98	7.43	364.19	1.92	27.26	22.53	7.15×10^3	0.85	0.26	8.44	1.44	5.07±0.20	0.31	-	86.82
-241	41.04	7.50	364.14	1.94	19.17	17.99	1.03×10^4	1.21	0.31	8.50	1.45	5.02±0.10	1.56	-	32.06
-270	41.18	7.82	364.44	2.02	15.87	16.13	1.29×10^4	1.49	0.35	8.68	1.48	4.82±0.08	1.59	-	66.79
-301	41.30	8.06	364.02	2.09	13.18	14.43	1.60×10^4	1.82	0.39	8.81	1.50	4.67±0.09	1.18	-	46.75
-447	39.96	8.24	296.14	2.12	6.09	8.69	3.53×10^4	3.99	0.58	8.87	1.52	3.71±0.05	1.33	-	46.74
-598	38.79	8.17	245.93	2.09	3.38	5.82	6.26×10^4	7.15	0.78	8.76	1.51	3.11±0.04	0.90	-	53.41
-693	38.39	7.72	196.48	1.97	2.38	4.50	8.41×10^4	9.89	0.90	8.51	1.47	2.63±0.03	0.53	-	100.15

TABLE 5. Data and output parameters from the study of the precessional modes' evolution. In all the cases above, $\Gamma = 2$, $Pm = 1.71 \times 10^{-6}$, and $Pr = 0.025$. In this table, B is the magnetic flux density; \bar{T} is the average temperature of the top and bottom plates; ΔT is the temperature drop across the tank height; P is the net power input with heat loss correction; Ra_A^∞ and Ra_W^∞ are critical Ra predictions from Chandrasekhar's asymptotic solution for an infinite plane (Chandrasekhar 1961) and Busse's asymptotic solution for a semi-infinite plane with a vertical wall (Busse 2008); Ch is the Chandrasekhar number; N_C is the convective interaction parameter; N_{TE} is the thermoelectric interaction parameter, defined in eq. (2.23); Rm is the free-fall estimate of the magnetic Reynolds number; Nu is the Nusselt number; f/f_κ is the peak frequency of the averaged spectrum over six sidewall thermistors, normalized by thermal diffusion frequency; f_{jrv}/f_κ is the jump-rope vortex frequency, normalized by thermal diffusion frequency; and t/τ_κ is time normalized by $\tau_\kappa = H^2/\kappa$, after the time series data reached statistical equilibrium. Prior to the acquisition of the data, each case is equilibrated for at least 30 min, which is over $2\tau_\kappa$.

REFERENCES

- ABDOU, M. A., YING, A., MORLEY, N., GULEC, K., SMOLENTSEV, S., KOTSCHENREUTHER, M., MALANG, S., ZINKLE, S., ROGNLIEN, T., FOGARTY, P. & NELSON, B. 2001 On the exploration of innovative concepts for fusion chamber technology. *Fusion Eng. Des.* **54** (2), 181–247.
- AHLERS, G., GROSSMANN, S. & LOHSE, D. 2009 Heat transfer and large scale dynamics in turbulent Rayleigh–Bénard convection. *Rev. Mod. Phys.* **81** (2), 503.
- AKHMEDAGAEV, R., ZIKANOV, O., KRASNOV, D. & SCHUMACHER, J. 2020 Turbulent Rayleigh–Bénard convection in a strong vertical magnetic field. *J. Fluid Mech.* **895**.
- AURNOU, J. M., BERTIN, V., GRANNAN, A. M., HORN, S. & VOGT, T. 2018 Rotating thermal convection in liquid gallium: Multi-modal flow, absent steady columns. *J. Fluid Mech.* **846**, 846–876.
- AURNOU, J. M., CALKINS, M. A., CHENG, J. S., JULIEN, K., KING, E. M., NIEVES, D., SODERLUND, K. M. & STELLMACH, S. 2015 Rotating convective turbulence in earth and planetary cores. *Phys. Earth Planet. Inter.* **246**, 52–71.
- AURNOU, J. M. & KING, E. M. 2017 The cross-over to magnetostrophic convection in planetary dynamo systems. *Proc. Math. Phys. Eng. Sci.* **473** (2199), 20160731.
- AURNOU, J. M. & OLSON, P. L. 2001 Experiments on Rayleigh–Bénard convection, magnetoconvection and rotating magnetoconvection in liquid gallium. *J. Fluid Mech.* **430**, 283–307.
- BARLEON, L., CASAL, V. & LENHART, L. 1991 MHD flow in liquid-metal-cooled blankets. *Fusion Eng. Des.* **14** (3-4), 401–412.
- BOETTINGER, W. J., CORIELL, S. R., GREER, A. L., KARMA, A., KURZ, W., RAPPAZ, M. & TRIVEDI, R. 2000 Solidification microstructures: recent developments, future directions. *Acta Mater.* **48** (1), 43–70.
- BOUSSINESQ, J. 1903 *Theorie Analytique de la Chaleur vol 2*. (Paris: Gauthier-Villars).
- BROWN, E. & AHLERS, G. 2006 Effect of the Earth’s Coriolis force on the large-scale circulation of turbulent Rayleigh–Bénard convection. *Phys. Fluids* **18** (12), 125108.
- BROWN, E. & AHLERS, G. 2007 Large-scale circulation model for turbulent Rayleigh–Bénard convection. *Phys. Rev. Lett.* **98** (13), 134501.
- BROWN, E. & AHLERS, G. 2009 The origin of oscillations of the large-scale circulation of turbulent Rayleigh–Bénard convection. *J. Fluid Mech.* **638**, 383–400.
- BUFFETT, B. A. & SEAGLE, C. T. 2010 Stratification of the top of the core due to chemical interactions with the mantle. *J. Geophys. Res. Solid Earth* **115** (B4).
- BUNGE, H. 2005 Low plume excess temperature and high core heat flux inferred from non-adiabatic geotherms in internally heated mantle circulation models. *Phys. Earth Planet. Inter.* **153** (1-3), 3–10.
- BUSSE, F. H. 2008 Asymptotic theory of wall-attached convection in a horizontal fluid layer with a vertical magnetic field. *Phys. Fluids* **20** (2), 024102.
- CASTRO-TIRADO, A. J., DE UGARTE POSTIGO, A., GOROSABEL, J., JELÍNEK, M., FATKHULLIN, T. A., SOKOLOV, V. V., FERRERO, P., KANN, D. A., KLOSE, S., SLUSE, D. & OTHERS 2008 Flares from a candidate galactic magnetar suggest a missing link to dim isolated neutron stars. *Nature* **455** (7212), 506.
- CHANDRASEKHAR, S. 1961 *Hydrodynamic and hydromagnetic stability*. Courier Corporation.
- CHEN, L., CHEN, P., LI, W., ZHANG, Q., STRUZHKIN, V. V., GONCHAROV, A. F., REN, Z. & CHEN, X. 2019 Enhancement of thermoelectric performance across the topological phase transition in dense lead selenide. *Nat. Mater.* **18** (12), 1321–1326.
- CHENG, J. S. & AURNOU, J. M. 2016 Tests of diffusion-free scaling behaviors in numerical dynamo datasets. *Earth Planet. Sci. Lett.* **436**, 121–129.
- CHENG, J. S., WANG, B., MOHAMMAD, I., FORER, J. M. & KELLEY, D. H. 2021 Laboratory model of electrovortex flow with thermal gradients, for liquid metal batteries. *arXiv preprint arXiv:2108.01648* .
- CHILLÀ, F. & SCHUMACHER, J. 2012 New perspectives in turbulent Rayleigh–Bénard convection. *Eur. Phys. J. E* **35** (7), 58.
- CIONI, S., CHAUMAT, S. & SOMMERIA, J. 2000 Effect of a vertical magnetic field on turbulent Rayleigh–Bénard convection. *Phys. Rev. E* **62** (4), R4520.
- CIONI, S., CILIBERTO, SERGIO & SOMMERIA, JÖEL 1997 Strongly turbulent Rayleigh–Bénard

- convection in mercury: comparison with results at moderate prandtl number. *J. Fluid Mech.* **335**, 111–140.
- CLEVER, R. M. & BUSSE, F. H. 1981 Low-Prandtl-number convection in a layer heated from below. *J. Fluid Mech.* **102**, 61–74.
- COTTAAR, S. & LEKIC, V. 2016 Morphology of seismically slow lower-mantle structures. *Geophys. suppl. mon. not. R. Astron. Soc.* **207** (2), 1122–1136.
- CUSACK, N. E. 1963 The electronic properties of liquid metals. *Rep. Prog. Phys.* **26** (1), 361.
- DAVIDSON, P. A. 2016 *Introduction to Magnetohydrodynamics*, 2nd edn. *Cambridge Texts in Applied Mathematics* 1. Cambridge University Press.
- DAVIDSON, P. A. 1999 Magnetohydrodynamics in materials processing. *Annu. Rev. Fluid Mech.* **31** (1), 273–300.
- DESCHAMPS, F., ROGISTER, Y. & TACKLEY, P. J. 2018 Constraints on core–mantle boundary topography from models of thermal and thermochemical convection. *Geophys. J. Int.* **212** (1), 164–188.
- ECKE, R. E., ZHONG, F. & KNOBLOCH, E. 1992 Hopf bifurcation with broken reflection symmetry in rotating Rayleigh–Bénard convection. *EPL* **19** (3), 177.
- FINLAY, C. C. 2008 Course 8: Waves in the presence of magnetic fields, rotation and convection. In *Les Houches*, , vol. 88, pp. 403–450. Elsevier.
- FINLAY, C. C., OLSEN, N., KOTSIAROS, S., GILLET, N. & TÖFFNER-CLAUSEN, L. 2016 Recent geomagnetic secular variation from swarm and ground observatories as estimated in the chaos-6 geomagnetic field model. *Earth Planets Space* **68** (1), 1–18.
- FULKERSON, W., MOORE, J. P., WILLIAMS, R. K., GRAVES, R. S. & MCELROY, D. L. 1968 Thermal conductivity, electrical resistivity, and Seebeck coefficient of silicon from 100 to 1300 k. *Phys. Rev* **167** (3), 765.
- FUNFSCHILLING, DENIS & AHLERS, GUENTER 2004 Plume motion and large-scale circulation in a cylindrical Rayleigh–Bénard cell. *Phys. Rev. Lett.* **92** (19), 194502.
- FUNFSCHILLING, D., BROWN, E. & AHLERS, G. 2008 Torsional oscillations of the large-scale circulation in turbulent Rayleigh–Bénard convection. *J. Fluid Mech.* **607**, 119.
- GARNERO, E. J., MCNAMARA, A. K. & SHIM, S. 2016 Continent-sized anomalous zones with low seismic velocity at the base of earth’s mantle. *Nat. Geosci.* **9** (7), 481–489.
- GARNERO, E. J., REVENAUGH, J., WILLIAMS, Q., LAY, T. & KELLOGG, L. H. 1998 Ultralow velocity zone at the core–mantle boundary. *The core–mantle boundary region* **28**, 319–334.
- GIAMPIERI, G. & BALOGH, A. 2002 Mercury’s thermoelectric dynamo model revisited. *Planet. Space Sci.* **50** (7–8), 757–762.
- GLAZIER, J. A., SEGAWA, T., NAERT, A. & SANO, M. 1999 Evidence against ‘ultrahard’ thermal turbulence at very high Rayleigh numbers. *Nature* **398** (6725), 307–310.
- GOLUSKIN, D., JOHNSTON, H., FLIERL, G. R. & SPIEGEL, E. A. 2014 Convectively driven shear and decreased heat flux. *J. Fluid Mech.* **759**, 360–385.
- GRANNAN, A. M., VOGT, T., HORN, S., HAWKINS, E. K., AGGARWAL, A. & AURNOU, J. M. 2017 Behaviors and transitions along the path to magnetostrophic convection. In *AGU Fall Meeting Abstracts*.
- GRAY, D. D. & GIORGINI, A. 1976 The validity of the boussinesq approximation for liquids and gases. *Int. J. Heat Mass Transf.* **19** (5), 545–551.
- GROSSMANN, S. & LOHSE, D. 2004 Fluctuations in turbulent Rayleigh–Bénard convection: the role of plumes. *Phys. Fluids* **16** (12), 4462–4472.
- HOLME, R. 2015 Large-scale flow in the core. *Treatise on Geophysics* **8**, 107–130.
- HOLMSTRÖM, E., STIXRUDE, L., SCIPIONI, R. & FOSTER, A. S. 2018 Electronic conductivity of solid and liquid (Mg, Fe)O computed from first principles. *Earth Planet. Sci. Lett.* **490**, 11–19.
- HORI, K., JONES, C. A. & TEED, R. J. 2015 Slow magnetic Rossby waves in the Earth’s core. *Geophys. Res. Lett.* **42** (16), 6622–6629.
- HORN, S. & SHISHKINA, O. 2015 Toroidal and poloidal energy in rotating Rayleigh–Bénard convection. *J. Fluid Mech.* **762**, 232–255.
- HOUCHEMS, B. C., WITKOWSKI, L. M. & WALKER, J. S. 2002 Rayleigh–Bénard instability in a vertical cylinder with a vertical magnetic field. *J. Fluid Mech.* **469**, 189–207.
- JAWORSKI, M. A., GRAY, T. K., ANTONELLI, M., KIM, J. J., LAU, C. Y., LEE, M. B.,

- NEUMANN, M. J., XU, W. & RUZIC, D. N. 2010 Thermoelectric magnetohydrodynamic stirring of liquid metals. *Phys. Rev. Lett.* **104** (9), 094503.
- JONES, C. A. 2011 Planetary magnetic fields and fluid dynamos. *Annu. Rev. Fluid Mech.* **43**, 583–614.
- JULIEN, K., LEGG, S., MCWILLIAMS, J. & WERNE, J. 1996 Rapidly rotating turbulent Rayleigh–Bénard convection. *J. Fluid Mech.* **322**, 243–273.
- KAO, A., PERICLEOUS, K., PATEL, M. K. & VOLLER, V. 2009 Effects of magnetic fields on crystal growth. *Int. J. Cast Met. Res.* **22** (1–4), 147–150.
- KASAP, S. 2001 Thermoelectric effects in metals: thermocouples. *Canada: Department of Electrical Engineering University of Saskatchewan*.
- KELLEY, D. H. & WEIER, T. 2018 Fluid mechanics of liquid metal batteries. *Appl. Mech. Rev.* **70** (2).
- KING, E. M. & AURNOU, J. M. 2015 Magnetostrophic balance as the optimal state for turbulent magnetoconvection. *Proc. Natl. Acad. Sci. U.S.A.* **112** (4), 990–994.
- KING, E. M., STELMACH, S. & AURNOU, J. M. 2012 Heat transfer by rapidly rotating Rayleigh–Bénard convection. *J. Fluid Mech.* **691**, 568–582.
- KNAEPEN, B. & MOREAU, R. 2008 Magnetohydrodynamic turbulence at low magnetic Reynolds number. *Annu. Rev. Fluid Mech.* **40**, 25–45.
- KUNNEN, R. P. J., CLERCX, H. J. H. & GEURTS, B. J. 2008 Breakdown of large-scale circulation in turbulent rotating convection. *Euro. Phys. Lett.* **84** (2), 24001.
- LANDAU, L. D. & LIFSHITZ, E. M. 1976 Theoretical physics. vol. 1. *Mechanics. Moscow, Nauka*.
- LAY, T., WILLIAMS, Q. & GARNERO, E. J. 1998 The core–mantle boundary layer and deep earth dynamics. *Nature* **392** (6675), 461–468.
- LI, M., MCNAMARA, A. K., GARNERO, E. J. & YU, S. 2017 Compositionally-distinct ultra-low velocity zones on earth’s core–mantle boundary. *Nat. Commun* **8** (1), 1–9.
- LIU, J., LI, J., HRUBIAK, R. & SMITH, J. S. 2016 Origins of ultralow velocity zones through slab-derived metallic melt. *Proc. Natl. Acad. Sci. U.S.A.* **113** (20), 5547–5551.
- LIU, W., KRASNOV, D. & SCHUMACHER, J. 2018 Wall modes in magnetoconvection at high Hartmann numbers. *J. Fluid Mech.* **849**.
- MAO, H., HU, Q., YANG, L., LIU, J., KIM, D. Y., MENG, Y., ZHANG, L., PRAKAPENKA, V. B., YANG, W. & MAO, W. L. 2017 When water meets iron at Earth’s core–mantle boundary. *Natl. Sci. Rev.* **4** (6), 870–878.
- MEDURI, D. G., BIGGIN, A. J., DAVIES, C. J., BONO, R. K., SPRAIN, C. J. & WICHT, J. 2020 Numerical dynamo simulations reproduce palaeomagnetic field behaviour. *Geophys. Res. Lett.* p. e2020GL090544.
- MERRILL, R. T. & MCELHINNY, M. W. 1977 Anomalies in the time-averaged paleomagnetic field and their implications for the lower mantle. *Rev. Geophys.* **15** (3), 309–323.
- MOFFATT, K. & DORMY, E. 2019 Self-Exciting Fluid Dynamos **59**.
- MOREAU, R. 1999 The fundamentals of MHD related to crystal growth. *Prog. Cryst. Growth Charact. Mater.* **38** (1–4), 161–194.
- MOROZOVA, N. V., KORBEINIKOV, I. V. & OVSYANNIKOV, S. V. 2019 Strategies and challenges of high-pressure methods applied to thermoelectric materials. *J. Appl. Phys.* **125** (22), 220901.
- MOSCA, I., COBDEN, L., DEUSS, A., RITSEMA, J. & TRAMPERT, J. 2012 Seismic and mineralogical structures of the lower mantle from probabilistic tomography. *J. Geophys. Res. Solid Earth* **117** (B6).
- MOTT, N. F. & JONES, H. 1958 *The theory of the properties of metals and alloys*. Dover.
- MOUND, J., DAVIES, C., ROST, S. & AURNOU, J. 2019 Regional stratification at the top of earth’s core due to core–mantle boundary heat flux variations. *Nat. Geosci.* **12** (7), 575–580.
- NAKAGAWA, Y. 1955 An experiment on the inhibition of thermal convection by a magnetic field. *Nature* **175** (4453), 417.
- OBERBECK, A. 1879 Ueber die Wärmeleitung der Flüssigkeiten bei Berücksichtigung der Strömungen infolge von Temperaturdifferenzen. *Ann. Phys* **243** (6), 271–292.
- PANDEY, A., SCHEEL, J. D. & SCHUMACHER, J. 2018 Turbulent superstructures in Rayleigh–Bénard convection. *Nat. Commun.* **9** (1), 1–11.

- PROCTOR, M. R. E. & WEISS, N. O. 1982 Magnetoconvection. *Rep. Prog. Phys.* **45** (11), 1317.
- REMPEL, M., SCHÜSSLER, M. & KNÖLKER, M. 2009 Radiative magnetohydrodynamic simulation of sunspot structure. *Astrophys. J.* **691** (1), 640.
- ROBERTS, P. H. & KING, E. M. 2013 On the genesis of the Earth's magnetism. *Rep. Prog. Phys.* **76** (9), 096801.
- RUDOLPH, P. 2008 Travelling magnetic fields applied to bulk crystal growth from the melt: The step from basic research to industrial scale. *J. Cryst. Growth* **310** (7-9), 1298–1306.
- SALAVY, J. F., BOCCACCINI, L. V., LÄSSER, R., MEYDER, R., NEUBERGER, H., POITEVIN, Y., RAMPAL, G., RIGAL, E., ZMITKO, M. & AIELLO, A. 2007 Overview of the last progresses for the european test blanket modules projects. *Fusion Eng. Des.* **82** (15-24), 2105–2112.
- SARRIS, I. E., ZIKOS, G. K., GRECOS, A. P. & VLACHOS, N. S. 2006 On the limits of validity of the low magnetic Reynolds number approximation in MHD natural-convection heat transfer. *Numer. Heat Tr. B-Fund.* **50** (2), 157–180.
- SCHMITT, D., CARDIN, P., LA RIZZA, P. & NATAF, H. C. 2013 Magneto–Coriolis waves in a spherical Couette flow experiment. *Eur. J. Mech. B. Fluids* **37**, 10–22.
- SCHNEIDER, D. A. & KENT, D. V. 1988 Inclination anomalies from indian ocean sediments and the possibility of a standing nondipole field. *J. Geophys. Res. Solid Earth* **93** (B10), 11621–11630.
- SCHÜSSLER, M. & VÖGLER, A. 2006 Magnetoconvection in a sunspot umbra. *Astrophys. J. Lett.* **641** (1), L73.
- SHERCLIFF, J. A. 1979 Thermoelectric magnetohydrodynamics. *J. Fluid Mech.* **91** (2), 231–251.
- STEVENS, R. J. A. M., BLASS, A.R, ZHU, X., VERZICCO, R. & LOHSE, D. 2018 Turbulent thermal superstructures in Rayleigh–Bénard convection. *Phys. Rev. Fluid* **3** (4), 041501.
- STEVENSON, D. J. 1987 Mercury's magnetic field: a thermoelectric dynamo? *Earth Planet. Sci. Lett.* **82** (1-2), 114–120.
- SUN, C., XIA, K. & TONG, P. 2005 Three-dimensional flow structures and dynamics of turbulent thermal convection in a cylindrical cell. *Phys. Rev.* **72** (2), 026302.
- TABERLET, E. & FAUTRELLE, Y. 1985 Turbulent stirring in an experimental induction furnace. *J. Fluid Mech.* **159**, 409–431.
- TAN, E., GURNIS, M. & HAN, L. 2002 Slabs in the lower mantle and their modulation of plume formation. *Geochem. Geophys. Geosystems* **3** (11), 1–24.
- TASAKA, Y., IGAKI, K., YANAGISAWA, T., VOGT, T., ZUERNER, T. & ECKERT, S. 2016 Regular flow reversals in Rayleigh–Bénard convection in a horizontal magnetic field. *Phys. Rev. E* **93** (4), 043109.
- TERASAKI, I. 2011 1.09 thermal conductivity and thermoelectric power of semiconductors. *Semicond. Sci. Technol.* p. 326.
- THORNE, M. S., LENG, K., PACHHAI, S., ROST, S., WICKS, J. & NISSEN-MEYER, T. 2021 The most parsimonious ultralow-velocity zone distribution from highly anomalous spdks waveforms. *Geochem. Geophys. Geosystems* **22** (1), e2020GC009467.
- THORNE, M. S., PACHHAI, S., LENG, K., WICKS, J. K. & NISSEN-MEYER, T. 2020 New candidate ultralow-velocity zone locations from highly anomalous spdks waveforms. *Minerals* **10** (3), 211.
- THUAL, O. 1992 Zero-Prandtl-number convection. *J. Fluid Mech.* **240**, 229–258.
- TRAMPERT, J., DESCHAMPS, F., RESOVSKY, J. & YUEN, D. 2004 Probabilistic tomography maps chemical heterogeneities throughout the lower mantle. *Science* **306** (5697), 853–856.
- TRITTON, D. J. 1977 *Physical Fluid Dynamics*. Springer Science & Business Media.
- VERZICCO, R. 2004 Effects of nonperfect thermal sources in turbulent thermal convection. *Phys. Fluids* **16** (6), 1965–1979.
- VOGT, T., HORN, S. & AURNOU, J. M 2021 Oscillatory thermal–inertial flows in liquid metal rotating convection. *J. Fluid Mech.* **911**.
- VOGT, T., HORN, S., GRANNAN, A. M. & AURNOU, J. M. 2018a Jump rope vortex in liquid metal convection. *Proc. Natl. Acad. Sci. U.S.A.* **115** (50), 12674–12679.
- VOGT, T., ISHIMI, W., YANAGISAWA, T., TASAKA, Y., SAKURABA, A. & ECKERT, S. 2018b Transition between quasi-two-dimensional and three-dimensional Rayleigh–Bénard convection in a horizontal magnetic field. *Phys. Rev. Fluid* **3** (1), 013503.

- VON HARDENBERG, J., PARODI, A., PASSONI, G., PROVENZALE, A. & SPIEGEL, E. A. 2008 Large-scale patterns in Rayleigh-Bénard convection. *Phys. Lett.* **372** (13), 2223–2229.
- WEISS, N. O. & PROCTOR, M. R. E. 2014 *Magnetoconvection*. Cambridge University Press.
- XI, H., LAM, S. & XIA, K. 2004 From laminar plumes to organized flows: the onset of large-scale circulation in turbulent thermal convection. *J. Fluid Mech.* **503**, 47.
- XI, H., ZHOU, S., ZHOU, Q., CHAN, T. & XIA, K. 2009 Origin of the temperature oscillation in turbulent thermal convection. *Phys. Rev. Lett.* **102** (4), 044503.
- XIA, K., SUN, C. & ZHOU, S. 2003 Particle image velocimetry measurement of the velocity field in turbulent thermal convection. *Phys. Rev.* **68** (6), 066303.
- YAN, M., CALKINS, M. A., MAFFEI, S., JULIEN, K., TOBIAS, S. M. & MARTI, P. 2019 Heat transfer and flow regimes in quasi-static magnetoconvection with a vertical magnetic field. *J. Fluid Mech.* **877**, 1186–1206.
- YOSHINO, T., WANG, R., GOMI, H. & MORI, Y. 2020 Measurement of the seebeck coefficient under high pressure by dual heating. *Rev. Sci. Instrum.* **91** (3), 035115.
- ZHANG, X., CRAMER, A., LANGE, A. & GERBETH, G. 2009 Model experiments on macroscopic thermoelectromagnetic convection. *Magnetohydrodynamics* **45** (1), 25–42.
- ZHOU, Q., XI, H., ZHOU, S., SUN, C. & XIA, K. 2009 Oscillations of the large-scale circulation in turbulent Rayleigh-Bénard convection: the sloshing mode and its relationship with the torsional mode. *J. Fluid Mech.* **630**, 367.
- ZÜRNER, T., LIU, W., KRASNOV, D. & SCHUMACHER, J. 2016 Heat and momentum transfer for magnetoconvection in a vertical external magnetic field. *Phys. Rev. E* **94** (4), 043108.
- ZÜRNER, T., SCHINDLER, F., VOGT, T., ECKERT, S. & SCHUMACHER, J. 2019 Combined measurement of velocity and temperature in liquid metal convection. *J. Fluid Mech.* **876**, 1108–1128.
- ZÜRNER, T., SCHINDLER, F., VOGT, T., ECKERT, S. & SCHUMACHER, J. 2020 Flow regimes of Rayleigh-Bénard convection in a vertical magnetic field. *J. Fluid Mech.* **894**.